

# Improved ELMv1-ECA Simulations of Zero-Curtain Periods and Cold-season CH<sub>4</sub> and CO<sub>2</sub> Emissions at Alaskan Arctic Tundra Sites

Jing Tao<sup>1,2</sup>, Qing Zhu<sup>1</sup>, William J. Riley<sup>1</sup>, Rebecca B. Neumann<sup>2</sup>

<sup>1</sup>Climate and Ecosystem Sciences Division, Lawrence Berkeley National Laboratory, Berkeley, CA, 94720, USA

5 <sup>2</sup>Department of Civil and Environmental Engineering, University of Washington, Seattle, WA, 98195, USA

*Correspondence to:* Jing Tao (JingTao@lbl.gov)

**Abstract.** Field measurements have shown that cold-season methane (CH<sub>4</sub>) and carbon dioxide (CO<sub>2</sub>) emissions contribute a substantial portion to the annual net carbon emissions in permafrost regions. However, most earth system land models do not accurately reproduce cold-season CH<sub>4</sub> and CO<sub>2</sub> emissions, especially over the shoulder (i.e., thawing and freezing) seasons.

10 Here we use the Energy Exascale Earth System Model (E3SM) land model version 1 (ELMv1-ECA) to tackle this challenge and fill the knowledge gap of how cold-season CH<sub>4</sub> and CO<sub>2</sub> emissions contribute to the annual totals at Alaska Arctic tundra sites. Specifically, we improved the ELMv1-ECA soil water phase-change scheme, environmental controls on microbial activity, and cold-season methane transport module. Results demonstrate that both soil temperature and the duration of zero-curtain periods (i.e., the fall period when soil temperatures linger around 0°C) simulated by the updated ELMv1-ECA were

15 greatly improved, e.g., the Mean Absolute Error (MAE) in zero-curtain durations at 12 cm depth was reduced by 62% on average. Furthermore, the MAE of simulated cold-season carbon emissions at three tundra sites were improved by 72% and 70% on average for CH<sub>4</sub> and CO<sub>2</sub>, respectively. Overall, CH<sub>4</sub> emitted during the early cold season (Sep. and Oct.), which often includes most of the zero-curtain period in Arctic tundra, accounted for more than 50% of the total emissions throughout the entire cold season (Sep. to May) in the model, compared with around 49.4% (43-58%) in observations. From 1950 to 2017,

20 both CO<sub>2</sub> emissions during soil zero-curtain period and during the entire cold season showed increasing trends, for example, of 0.17 gC m<sup>-2</sup> year<sup>-1</sup> and 0.36 gC m<sup>-2</sup> year<sup>-1</sup> at Atqasuk. This study highlights the importance of zero-curtain periods in facilitating CH<sub>4</sub> and CO<sub>2</sub> emissions from tundra ecosystems.

## 1 Introduction

25 Cold-season carbon emissions from the Arctic tundra could potentially offset warm-season net carbon uptake under 21<sup>st</sup>  
century warming climate (Commane et al., 2017; Oechel et al., 2014; Oechel et al., 2000; Koven et al., 2011; Piao et al., 2008;  
Natali et al., 2019; Belshe et al., 2013; Fahnestock et al., 1998; Jones et al., 1999). Field measurements have indicated large  
cold-season CO<sub>2</sub> losses over Arctic tundra ecosystems (Oechel et al., 2014; Natali et al., 2019). Also, CH<sub>4</sub> emitted from  
September to May were found to contribute more than 50% of the annual total CH<sub>4</sub> emissions from Alaska upland tundra sites  
30 (Zona et al., 2016; Taylor et al., 2018). Despite the importance of cold-season carbon emissions and their sensitivity to  
changing climate, prevailing earth system land models do not accurately reproduce cold-season CH<sub>4</sub> and CO<sub>2</sub> emissions and  
their contributions to the annual budgets, largely because of the poorly understood mechanisms of cold-season soil  
heterotrophic respiration and therefore uncertain numerical representations (Natali et al., 2019; Zona et al., 2016; Wang et al.,  
2019; Commane et al., 2017). Thus, it remains challenging to assess the response of permafrost carbon dynamics to Arctic  
35 warming and to predict future annual carbon budgets with current Earth System Models (ESMs).

In ESM land models, soil environment influences soil microbial heterotrophic respiration (HR) and decomposition of soil  
organic carbon (SOC) mainly through applying prescribed temperature and moisture functions to modify base decomposition  
rates. These functions, however, rely heavily on empirical or semi-empirical relationships which are highly uncertain (Sierra  
40 et al., 2017; Sierra et al., 2015; Yan et al., 2018; Moyano et al., 2013; Tang and Riley, 2019; Rafique et al., 2016; Bhanja and  
Wang, 2020; Kim et al., 2019). Specifically, the temperature sensitivities of soil carbon decomposition is often represented  
with a  $Q_{10}$  value (i.e., the increase in respiration rate from a 10°C increase in temperature) that is fixed at 1.5 or 2.0 (Meyer et  
al., 2018). However, the values of  $Q_{10}$  are controversial (Davidson and Janssens, 2006). Some studies found a uniform  $Q_{10}$   
across biomes and climate zones, e.g., as 1.4 (Mahecha et al., 2010). Other studies demonstrated that  $Q_{10}$  varies with  
45 environmental conditions, ecosystem types, and soil texture (Meyer et al., 2018; Graf et al., 2011; Kim et al., 2019), showing  
a large spatial heterogeneity with generally higher values in the high-latitude regions (Zhou et al., 2009). In addition,  
Wilkman et al. (2018) reported a temporal heterogeneity in  $Q_{10}$  over the Alaskan Arctic Tundra and suggested a higher value  
(e.g., 2.45) for early summer (e.g., June) but lower value (e.g., 1.58 to 1.67) for the peak growing season (e.g., July). Dynamic  
decomposition temperature sensitivities are also consistent with theory of microbial dynamics (Tang and Riley, 2015). Also,  
50 the response of HR to changes in soil moisture is commonly expressed by empirical relationships in ESMs, which vary  
substantially (Sierra et al., 2015; Yan et al., 2018; Moyano et al., 2013). Although in-situ measurements reveal that microbial  
respiration occurs under very cold conditions (e.g., even when soil temperature is lower than -15 °C) (Natali et al., 2019; Zona  
et al., 2016), most process-based models completely shut down microbial activity due to limited liquid water in freezing and  
subfreezing soils, and few modelling studies have closely investigated the HR-moisture relationships in frozen conditions.

55

The strong dependency of CO<sub>2</sub> and CH<sub>4</sub> emission on soil temperature and moisture in ESM land models (Riley et al., 2011; Koven et al., 2017; Lawrence et al., 2015) requires accurate estimates of these two closely related soil variables, especially in cold regions where both increases and decreases in soil temperature could lead to soil “drying” due to drainage or freezing processes. However, current land models tend to significantly underestimate soil temperature during the cold season over permafrost regions (Dankers et al., 2011; Tao et al., 2017; Nicolsky et al., 2007; Yang et al., 2018b). One possible reason is that while many land models account for latent heat released during soil water freezing, they do not treat and distribute this heat appropriately or/and do not simulate soil moisture correctly (Yang et al., 2018a; Nicolsky et al., 2007). Latent heat released during freezing might be sufficient to offset heat conduction towards the surface, thus maintaining the subsurface soil temperature around the freezing point (i.e., 0°C) for weeks or even months during the fall (i.e., the so-called Zero-Curtain Period; ZCP) (Outcalt et al., 1990). The ZCP conditions allow for continued soil heterotrophic respiration at notable rates, and thus CO<sub>2</sub> and CH<sub>4</sub> production and emissions from subsurface soils (Kittler et al., 2017; Arndt et al., 2019; Commane et al., 2017). For instance, Zona et al. (2016) reported that a substantial portion of cold season CH<sub>4</sub> emissions occurred during the ZCP from Alaskan upland tundra sites. Nevertheless, many land models cannot accurately capture the ZCP length due to inaccurately simulated soil moisture and/or inadequate representation of latent heat, thus underestimating soil temperature and cold-season CO<sub>2</sub> emissions (Commane et al., 2017) and CH<sub>4</sub> (Zona et al., 2016).

We hypothesize that the underestimation of modelled cold-season CO<sub>2</sub> and CH<sub>4</sub> emissions in ESMs land models primarily results from underestimated soil temperatures during the cold season, the poor representations of environmental controls on heterotrophic respiration in subfreezing soils, and the lack of appropriate representation of cold-season methane transport processes. Here we apply the Energy Exascale Earth System Model (E3SM) land model version 1, the Equilibrium Chemistry Approximation configuration (ELMv1-ECA) (Golaz et al., 2019; Zhu et al., 2019; Burrows et al., 2020) to explore these hypotheses. We apply ELMv1-ECA to (i) improve simulations of subsurface soil temperatures, ZCPs, and CO<sub>2</sub> and CH<sub>4</sub> emissions over the permafrost tundra ecosystem; (ii) investigate the underlying processes that influence cold-season carbon emissions from freezing and subfreezing soils, including source characterization and transport pathways; and (iii) estimate historical trends (from 1950 to present) of cold-season CO<sub>2</sub> and CH<sub>4</sub> emissions at multiple Alaskan tundra sites.

The paper is organized as follows: (1) We describe the study sites and the data used in the study. (2) We present the theoretical background of essential modules of ELMv1-ECA relevant to this study and our modifications to the model’s representations of phase-change, SOC decomposition, and methane dynamics. (3) We then describe the model configuration and experimental design. (4) We assess the modified phase-change scheme by comparing simulated soil temperatures and ZCPs against observations. (5) With the revised phase-change scheme, we analyze how the parameterization of decomposition schemes and methane module impact simulated CO<sub>2</sub> and CH<sub>4</sub> emissions at the site scale. (6) Finally, we summarize the main findings and discuss needed observations and model development to further improve predictability.

## 2 Study Sites and Data

90 We assembled daily observations of CO<sub>2</sub> and CH<sub>4</sub> fluxes from 2013 to 2017 at five eddy-covariance flux tower sites in Alaska's North Slope tundra (Figure 1) from the Arctic-Boreal Vulnerability Experiment (ABoVE) project (2015 - 2017) (Oechel and Kalthori, 2018) and Carbon in Arctic Reservoirs Vulnerability Experiment (CARVE) flight campaign (2013 - 2014) (Zona et al., 2016). The CARVE CO<sub>2</sub> measurements were not available at the data archive we used here; therefore, monthly winter-time CO<sub>2</sub> flux data at the same towers assembled by Natali et al. (2019) are included to complement CO<sub>2</sub> observations from  
95 2013 to 2014. The five sites include three eddy covariance (EC) towers at Barrow (i.e., the Barrow Environmental Observatory (BEO) tower, the Biocomplexity Experiment South (BES) tower, and the Climate Monitoring and Diagnostics Laboratory (CMDL) tower), one tower at Atqasuk (ATQ) and another at Ivotuk (IVO) which is located at the foothills of the Brooks Range. BES and CMDL are collocated with each other with sensors installed at different heights (i.e., 2 m for BES and 5 m for CMDL). Vegetation at Barrow is mainly moist acidic tundra. Instrument height at ATQ and IVO is 2 m and 4 m,  
100 respectively. ATQ is a well-drained upland site, and the vegetation consists of moist-wet coastal sedge tundra and moist-tussock tundra surfaces. Vegetation at IVO is polar tundra. Table S1 provides basic information including geolocations, vegetation mosaic, and climatologic air temperature at the sites. (Tables numbered with a prefix “S” are include in the supplementary file, which will not be repeated in the following context throughout the manuscript.)

105 ABoVE and CARVE provide soil temperature and moisture measurements at various depths from 5 cm to 40 cm. The Permafrost Laboratory, Geophysical Institute of University of Alaska Fairbanks (GIPL-UAF), provides daily subsurface soil temperature observations down to various depths at permafrost sites across Alaska([http://permafrost.gi.alaska.edu/sites\\_map](http://permafrost.gi.alaska.edu/sites_map)) (Romanovsky et al., 2009). We used the GIPL-UAF permafrost sites that are collocated with the ABoVE sites to complement the ABoVE observations at deeper depths, including BR2 (down to 15 m) and IV4 (down to 1 m). We first filled missing gaps  
110 vertically by fitting a polynomial to the soil temperature profile (Kurylyk and Hayashi, 2016) on a daily scale, then screened out outliers by examining the daily time series. Further, we aggregated both the ABoVE and the GIPL-UAF soil temperature measurements to ELMv1-ECA soil layer node depths using the inverse distance weighting method (Tao et al., 2017), and then averaged the two sets of aggregated observations. We used the assembled subsurface temperature observation datasets to evaluate the ELMv1-ECA simulated soil temperature profiles and the zero-curtain periods.

115

The observed soil moisture is only available at two or three depths that are quite different from model layer node-depths, and also show discontinuities in time. Thus, evaluating ELMv1-ECA simulated liquid water content was limited. We matched soil-moisture observations to the vertically closest model layer, and then evaluated the simulated volumetric fraction of soil liquid water content at layers for time periods during which observations were available. In addition, we used ABoVE soil moisture  
120 measurements to derive site-scale soil porosity and organic carbon content (see Section 3.2).

### 3 Methodology

#### 3.1 Modifications to E3SM Land Model (ELM)

125 The E3SM land model version 1 (ELMv1-ECA) couples essential biogeophysical and biogeochemical processes that solve terrestrial ecosystem energy, water, carbon, and nutrient dynamics (Golaz et al., 2019; Zhu et al., 2019). In the appendix, we describe in detail its subsurface soil thermodynamics, the carbon decomposition module, and the methane module that are of particular relevance to our study. Here we identify the potential problems of ELMv1-ECA that are responsible for the underestimation of cold-season CH<sub>4</sub> and CO<sub>2</sub> emissions and summarize the modifications made to ELMv1-ECA, emphasizing the model enhancements.

##### 130 3.1.1 Phase Change Scheme

We first improved ELMv1-ECA's numerical representation of coupled water and heat transport with freeze-thaw processes via improving the phase-change scheme. The freeze-thaw processes of soil water within ELMv1-ECA is simulated in a decoupled way, i.e., it solves soil temperatures ignoring the latent heat associated with phase change, determines the mass change of soil water required to adjust the initially solved soil temperature to the freezing point (i.e., 0°C;  $T_f$ ), adjusts the soil  
135 liquid and ice content by mass and energy conservation, and then readjusts temperatures after accounting for the heat deduction or compensation resulted from melting or freezing (see the detailed description in the Appendix A). The underlying assumption here is, taking the freezing process as an example, the available liquid water at the initially solved temperature ( $T_i^{n+1}$ ) will be completely frozen, releasing latent heat ( $H_i$ ) to bring up  $T_i^{n+1}$  back to  $T_f$ . Then, the estimated phase-change rate will be tuned down and the current temperature (i.e.,  $T_f$ ) will be readjusted if the to-be-increased ice mass is larger than the required mass  
140 change ( $-H_m$ ) (see (Eq. A4) in the Appendix A), which, however, only occasionally occurs. When the liquid water available to be frozen becomes small enough, the released latent heat is not sufficient to compensate for the required energy deficit ( $T_f - T_i^{n+1}$ ), and then the freezing process stops. Consequently, the model freezes soil water quickly, resulting in an underestimated duration of the soil water phase-change processes and the zero-curtain periods, and also cold-biased winter temperatures (Nicolsky et al., 2007; Yang et al., 2018a).

145

Here, we employed a phase-change efficiency and the temperature of the freezing-point depression to effectively solve the problem of overestimating phase-change rates within the current ELMv1-ECA modelling structure. These modification factors are explained below. The phase-change efficiency, introduced by Le Moigne et al. (2012) and adopted by Masson et al. (2013) and Yang et al. (2018a), introduces the dependency of available liquid water on the phase-change rate (Le Moigne et al., 2012).  
150 The phase-change efficiency for freezing,  $\varepsilon_{liq,i}^n$  (see (Eq. A9)), is identical to the degree of moisture saturation, or the volumetric fraction of soil liquid water content (i.e.,  $Sf_{liq,i}^n = \theta_{liq,i}^n / \theta_{sat,i}$  where  $\theta_{liq,i}^n$  is soil liquid water content and  $\theta_{sat,i}$  is

porosity). . We applied the phase-change efficiency to the initially estimated energy and mass change involved, i.e.,  $H_i$  and  $H_m$  (see (Eq. A4) in the Appendix) when freezing or thawing process occur.

155 As in Nicolsky et al. (2007) and Yang et al. (2018a), the occurrence of a phase-change process is then determined by the  
temperature of the freezing point depression (i.e., an virtual temperature, see (Eq. A10)) instead of  $T_f$ . The virtual freezing  
point depression temperature is reversely derived from the freezing point temperature-depression equation (Fuchs et al., 1978;  
Cary and Mayland, 1972). With an upper limit as  $T_f$ , the virtual temperature describes the lowest temperature that can hold  
current liquid water content in the freezing soils. That is, the soil temperature has to be lower than the current virtual  
160 temperature to allow the freezing process to occur further.

We describe in detail the revised phase-change scheme in the Appendix A. In short, we improved the phase-change scheme of  
ELMv1-ECA by incorporating two modifications: 1) applying a phase-change efficiency to implicitly account for the heat  
compensation/deduction to the system from latent heat released/absorbed by soil water freezing/melting, and 2) replacing the  
165 constant freezing point with the temperature of the freezing point depression, as a virtual temperature, to determine the  
occurrence of phase change in subfreezing soils.

### 3.1.2 Environmental Modifiers to the Decomposition Rate

We revisited ELMv1-ECA's representation for soil heterotrophic respiration dynamics in subfreezing soils and then scrutinized  
the environmental scalars of soil temperature and moisture. Within ELMv1-ECA's decomposition cascade model, the  
170 environmental factors that impact the decomposition rates of soil organic matter include soil temperature ( $f_T$ ), soil moisture  
( $f_W$ ), oxygen stress ( $f_O$ ) and a depth scalar ( $f_D$ ) (See Appendix B). Within freezing and subfreezing soils, the soil water  
potential is related to temperature through the freezing point depression equation (Niu and Yang, 2006). The current moisture  
factor  $f_W$ , therefore, will predict zero respiration rates for subfreezing soils given a specific lower limit of soil water potential  
 $\psi_{min}$  (-10 MPa; (Eq. B13)) (Oleson et al., 2013), as shown by Figure S1a in the supplementary file. We thus decreased the  
175  $\psi_{min}$  further to prevent zero respiration within the active layer when soil becomes subfreezing during cold-season months  
(Figure S1b) as long as the soil water potential  $\psi_i$  exceeds the prescribed  $\psi_{min}$ .

For wet soils, the factor that primarily limits the decomposition rates is oxygen availability (Sierra et al., 2017; Yan et al.,  
2018), since increases in soil moisture result in decreased dissolved oxygen. ELMv1-ECA approximates oxygen stress ( $f_O$ ) as  
180 a ratio of available oxygen to the demand by decomposers, which, however, is highly uncertain and unstable (Oleson et al.,  
2013). Some existing moisture scalars incorporate the oxygen stress together to account for the inhibition of decomposition in  
wet anoxic conditions, e.g., a moisture function proposed by Yan et al. (2018) and several functions tested in Sierra et al.  
(2015), including Standcarb (Harmon and Domingo, 2001), Daycent (Kelly et al., 2000), Skopp (Skopp et al., 1990), and

Moyano (Moyano et al., 2013). We thus also tested these existing moisture functions by replacing the original moisture scalar  
185 with them in the ELMv1-ECA. Particularly for the moisture function of Yan et al. (2018), we implemented it for each soil  
layer using the soil properties (i.e., porosity and clay content) of each layer, and also tested it with different shape parameters  
and optimal wetness thresholds. When using the moisture scalars with built-in oxygen stress within ELMv1-ECA, the total  
environmental impacts on decomposition, i.e.,  $f_{total} = f_T f_W f_O f_D$  will be modified accordingly as  $f_{total} = f_T f_W f_D$  to avoid  
double-counting of the oxygen stress.

190

ELMv1-ECA uses a  $Q_{10}$ -based standard exponential function to account for the temperature effect on SOC decomposition (Eq.  
B12), with  $Q_{10}$  as 1.5 and  $T_{ref}$  as 25°C. Here, rather than striving for a single value of  $Q_{10}$  or a spatial map of  $Q_{10}$  as discussed  
in the introduction, or a particular individual temperature function, we seek a group of environmental modifiers ( $f_{total}$ ) that  
can correctly represent moisture and temperature sensitivity on heterotrophic respiration. Specifically, we assembled and tested  
195 814 cases of  $f_{total}$  using the newly modified moisture scalars and a variety of other empirical moisture and temperature  
functions, as documented by Sierra et al. (2015) and Yan et al. (2018). A full list of the specific moisture and temperature  
scalars tested is provided in Table S2.

### 3.1.3 Cold-season Methane Process

200 The ELMv1-ECA methane model solves the reaction and diffusion equation for  $CH_4$  and  $O_2$  fluxes with the Crank-Nicholson  
method. It includes the representations of  $CH_4$  production, oxidation, and three pathways of transport, including aerenchyma  
tissues, ebullition, aqueous and gaseous diffusion (Riley et al. (2011)). A short description of the ELMV1-ECA methane  
module is provided in Appendix C. The ELMv1-ECA methane model has been found to underestimate cold-season methane  
emissions over northern wetlands (Xu et al., 2016). The modifications to the phase-change scheme impact simulations of soil  
205 water and heat transfer (3.1.1); the changes in environmental scaler affect substrate availability (3.1.2). Both (3.1.1) and (3.1.2)  
influence soil heterotrophic respiration, and could potentially lead to improvements in simulated  $CO_2$  and  $CH_4$  production, but  
not necessarily  $CH_4$  emissions which are also controlled by oxidation and transport mechanisms.

Here, we first modified the ELMV1-ECA  $CH_4$  transport mechanism in cold seasons by mimicking possible pathways for  $CH_4$   
210 emissions from freezing and subfreezing soils. Specifically, we mimicked the emissions from ice cracks by plant aerenchyma  
transport (Zona et al., 2016), approximating the gas diffusion through ice cracks to the similar mechanism of diffusion through  
the aerenchyma tissues. Although in-situ experiments demonstrated that during winter, produced  $CH_4$  in frozen soils is  
predominately emitted to the atmosphere through vascular plants aerenchyma tissues (e.g., Kim et al., 2007), here we integrate  
the possible transport pathways including ice cracks and remnants of aerenchyma tissues together through equation (Eq. C16).

215 Also, during the cold season over the tundra ecosystem, snow on the land surface provides strong resistance to  $CH_4$  transport  
to the atmosphere in ELMv1-ECA. But in reality, studies have shown methane can diffuse through snowpack at varying rates

(Kim et al., 2007). We thus decreased snow resistance at the upper boundary by introducing a new scale factor when snow is present (Appendix C).

220 Table 1 summarized all the specific modifications made to ELMv1-ECA. These modifications involve new parameters that  
are all tuneable and can be systematically optimized via calibration. Here, we seek to reproduce the first-order cold-season  
process relevant to this study with these default formation and values listed in Table 1. We also conducted sensitive tests on  
seven CH<sub>4</sub> parameterizations, including six parameterizations resulting from fractional three key variables and one  
parameterization scheme using all the tested values for the three variables (Table S3). The three CH<sub>4</sub> process-related parameters  
225 include two key variables in the original CH<sub>4</sub> model that have been reported having large uncertainty (Riley et al., 2011), i.e.,  
 $f_{CH_4}$  (a fraction of anaerobically mineralized carbon atoms becoming CH<sub>4</sub>; Eq. C14) and  $R_{o,max}$  (the maximum oxidation rate  
constant; Eq. C17), and the newly introduced variable  $\epsilon_{aere}$  (a factor representing remnants of aerenchyma tissues during cold  
seasons and possible pathways via ice cracks; Eq. C16). The sensitive tests on CH<sub>4</sub> process-related parameters were applied  
to model with identified carbon decomposition schemes that predicted good simulations of CO<sub>2</sub> flux (see section 3.3).

230

### 3.2 Climate Forcing, Model Configuration, and Experiment Design

We conducted transient simulations at 30-minute temporal resolution driven by climate forcing from 0.5°×0.5° CRU JRA  
(Harris, 2019) from 1901 to 2017 at the four Alaska tundra site locations. Before the transient simulation, we conducted a 200-  
year Accelerated Decomposition (AD) spin-up period followed by a 200-year regular spin-up period (Koven et al., 2013b; Zhu  
235 et al., 2019) to initialize land carbon pools. Spin-up simulations start from a wet and cold condition. Specifically, sub-surface  
temperatures were initialized as 274 K for the 1<sup>st</sup> to 5<sup>th</sup> soil layers, 273 K for the 6<sup>th</sup> to 10<sup>th</sup> layer, and 272 K for the 11<sup>th</sup> to the  
15<sup>th</sup> layer, and volumetric soil water content was initialized fully saturated for all layers. In this manner, consistent vertical soil  
water content profiles were built in over the permafrost regions.

240 Baseline simulations were conducted with ELMv1-ECA default physics, parameters, and surface datasets, i.e.,  
OriPC\_OriDecom\_OriCH4 using original phase-change scheme, original decomposition scheme and methane module (Table  
2). To improve the model representation of the site-level soil environment, we first examined the global soil organic matter  
data at the ABoVE sites by evaluating ELMv1-ECA simulated subsurface soil temperature with the topsoil temperature  
prescribed to observations (as did in Tao et al., 2017). Using the top soil layer as the upper boundary, the modelling system  
245 excluded potential errors induced by inaccurate meteorological forcing and vegetation cover that impact the simulation of heat  
transfer from the atmosphere to the shallow soil (Tao et al., 2017). Then, the accuracy of simulated soil subsurface temperature  
is directly determined by the factors impacting heat transfer along the “shallow-to-deep soil” gradient (Koven et al., 2013a),  
e.g., soil thermal properties which are mostly determined by SOC content (Tao et al., 2017; Lawrence and Slater, 2008).  
Results well reproduced the subsurface soil temperatures except at IVO, where summer soil temperatures were notably

250 overestimated (see Figure S2a). This result indicates that the SOC content at IVO was too small, leading to a large thermal conductivity, small soil porosity, and small heat capacity, altogether resulting in fast penetration of heat into the subsurface soil during summer (Tao et al., 2017; Lawrence and Slater, 2008). Thus, we derived the organic matter density at IVO based on ABoVE soil moisture data through a linear relationship between SOC content and soil porosity (i.e., Equation 3 in Lawrence and Slater (2008)), assuming the observed maximum volumetric water content was porosity (see Figure S3 for details). With  
255 the newly derived profile of soil organic matter density at IVO, the simulation showed large improvements in summer soil temperatures compared to that using the original global carbon dataset (see Figure S2b). The derived SOC content is also consistent with the soil survey data reported in Davidson and Zona (2018). Hereafter, the simulations at IVO presented in this paper use the newly derived organic carbon data without repeated clarification.

260 The representative spatial scale of the eddy flux tower is small compared to the grid cell of global surface datasets and the climate forcing data used by ELMv1-ECA, although the forcing dataset was interpolated to the site scale with a bilinear or nearest-neighbor method. The site-scale vegetation cover also shows a large diversity of vegetation types according to the detailed vegetation survey at ABoVE flux tower footprints obtained in 2014 (Davidson and Zona, 2018). The ELMv1-ECA's default plant type function (PFT) dataset was derived from satellite-based data by Lawrence et al. (2007). We analyzed the  
265 vegetation composition from the closet survey plot to the flux tower and examined the rationality of ELMv1-ECA's percentage of PFT for the site-scale simulation through testing different PFT datasets derived from this vegetation survey (Davidson and Zona, 2018). We found that these PFT datasets generally are not superior to the original PFT dataset, which generally reproduced satellite-based GPP (Figure S4). We thus confirmed that ELMv1-ECA's PFT dataset was a good compromise between representing the site-scale ecosystem and other global parameters and surface datasets within the model. The surface  
270 CH<sub>4</sub> emission is a weighted average of simulated saturated and unsaturated components using predicted inundation and non-inundation fractions. To compare simulated CH<sub>4</sub> emissions with ABoVE measurements at the site scale, we use the estimated inundation fractions at the footprint of ABoVE eddy-covariance flux towers (see details in (Xu et al., 2016)).

Table 2 lists the experiments conducted in this study. We modified each model component (i.e., the heat transfer model, carbon  
275 decomposition model, and methane model) serially. All the experiments ran through 1901 to 2017 with spin up as described earlier, although the evaluation and optimization were conducted only using results from 2013 to 2017. We first ran simulations with the 814 environmental modifiers together with the modified methane model with default parametrization (Table S3). Then, we selected the environmental modifiers that provided satisfactory performance in simulating CO<sub>2</sub> flux, and repeated simulations with the seven CH<sub>4</sub> parameterizations (Table S3). Among all the simulations results, we identified an optimal  
280 simulation for each site (see details in section 3.3).

### 3.3 Evaluation Metrics, Optimization Method, and Trend Analysis

We define the early cold season as September and October, the cold-season period as September to May which includes the two shoulder seasons (both thawing and freezing) as consistent with Zona et al. (2016), and the warm season from June to August. We define the zero-curtain period (ZCP) as the set of successive days when the soil temperature is within the range of  $[-0.75^{\circ}\text{C}, 0.75^{\circ}\text{C}]$  starting in fall (i.e., the freezing season) based on Zona et al. (2016). We computed the ZCP duration for each soil layer every year from 1950 to 2017 and estimated the historical trend as the regression slope between ZCP duration and time. Similarly, we estimated the trends of cold-season  $\text{CH}_4$  and  $\text{CO}_2$  emissions through linear regression analysis. A p-value of 0.05 is used to determine if the computed trend is statistically significant. Results vary with soil depths; thus, we choose a common modelling depth at which the ZCPs show significant trends for all the sites, to give an example.

To evaluate ELMv1-ECA simulated soil temperature and moisture, we calculated the RMSE for each soil layer, i.e.,  $\sqrt{\sum_{t=1}^N (\hat{E}_t - O_t)^2 / N}$  where the  $\hat{E}_t$  and  $O_t$  is simulated and observed soil temperature or moisture, respectively, and  $t$  is a daily time step. We used the Mean Absolute Error (MAE, i. e.,  $\frac{1}{N} \sum_{t=1}^N |\hat{E}_t - O_t|$ ) to assess the simulated duration of ZCP of each soil layer. Note that, depending on the amount of soil liquid water content, the whole course of the freezing process may or may not entirely fall into the ZCP, i.e., the ending time of ZCP does not necessarily align with the end of the freezing process. The onset of freezing, though, is always later than the starting day of the ZCP, and the main course of the freezing process is still within the ZCP.

Here the modelled active layer thickness (ALT), i.e., maximum thaw depth during an annual cycle, is computed as the bottom depth of the deepest thawed soil layer (i.e., with a maximum annual temperature above  $0^{\circ}\text{C}$ ) further extended down to the possible non-frozen fraction of the layer below, as in Tao et al. (2019; 2017). We only derived the length of ZCP for soil layers with a maximum annual temperature above  $0^{\circ}\text{C}$  since limited phase-change processes occur in deeper layers. Then, the soil layers containing or below the permafrost table have a zero-day ZCP. We computed the MAE of ALT simulated with both original (OriPC) and the new phase-change (NewPC) scheme. Also, we computed the relative improvement in simulated soil temperature (Ts) and ZCP compared to the baseline results. Specifically, we calculated  $100\% \times (\text{RMSE\_Ts\_OriPC} - \text{RMSE\_Ts\_NewPC}) / \text{RMSE\_Ts\_OriPC}$  and  $100\% \times (\text{MAE\_ZCP\_OriPC} - \text{MAE\_ZCP\_NewPC}) / \text{MAE\_ZCP\_OriPC}$  to quantify the enhancement by employing the new phase-change scheme.

We used Nash-Sutcliffe Efficiency (NSE) (Nash and Sutcliffe, 1970) to examine the performance of the ELMv1-ECA simulated time series of  $\text{CH}_4$  and  $\text{CO}_2$  net fluxes in comparison with assembled observations (Section 2) at the monthly time scale. The NSE ranges from negative infinity to one, calculated as Eq. (1):

$$NSE = 1 - \left( \frac{1}{N} \sum_{t=1}^N (\hat{E}_t - O_t)^2 \right) / \sigma_o^2, \quad (1)$$

where  $t$  means monthly time step,  $N$  is the total number of time steps,  $\hat{E}_t$  and  $O_t$  is simulated and observed flux at time step  $t$ , respectively; and  $\sigma_o$  is the standard deviation of observations. Note we only used observed monthly averages when the number of daily observations was more than 20 days. The model performance is generally considered satisfactory with an  $NSE > 0.50$  (Moriassi et al., 2007), and perfect with an  $NSE$  as one. To simultaneously evaluate  $CH_4$  and  $CO_2$  fluxes, we combined both  $NSE_{CH_4}$  and  $NSE_{CO_2}$  in the form of  $dist = \sqrt{(1 - NSE_{CH_4})^2 + (1 - NSE_{CO_2})^2}$ , representing the distance from  $(NSE_{CH_4}, NSE_{CO_2})$  to  $(1, 1)$  in a coordinate plane with x-axis as  $NSE_{CH_4}$  and y-axis as  $NSE_{CO_2}$ . Then, the optimal simulation thereby is the one having the shortest distance to the ideal scenario  $(1, 1)$ . We also define a satisfactory model performance in terms of simulating  $CH_4$  and  $CO_2$  fluxes as the case with both  $NSE_{CH_4}$  and  $NSE_{CO_2}$  larger than 0.5.

We optimized the model simulations through two steps. Specifically, we first evaluated the simulations using (814) environmental modifiers to the base decomposition rate that assembled commonly used empirical soil temperature- and moisture-dependency functions (Table S2). These simulations used the newly modified methane model with the default parameters (Table S3). We selected the common decomposition schemes that provided satisfactory results of  $CO_2$  flux for all the sites (i.e.,  $NSE_{CO_2} > 0.5$ ). Then, we iteratively repeated simulations with the common carbon decomposition schemes along with the seven  $CH_4$  parameterizations (Table S3). Among all these simulations (“NewPC\_NewDecomNewCH4”; Table 2), we identified an optimal simulation for each site that has the smallest distance from  $(NSE_{CH_4}, NSE_{CO_2})$  to  $(1, 1)$  (i.e.,  $dist$ ); the environmental modifier to the base decomposition rate and the methane parameterization used in the optimal simulation is the optimized parameterization for this site.

Further, among the common parameterizations of environmental modifiers and  $CH_4$  parameterizations that show satisfactory performance both in  $CH_4$  and  $CO_2$  fluxes for all the sites, we identified a generic scheme as the one providing the minimum Euclidean distance in a site-performance space, calculated as  $\sqrt{\sum_{i=1}^n dist_i^2}$  where  $n$  is number of sites. The generic scheme then is the common satisfactory scheme that provides the best overall performance for all the sites and can be applied for the regional simulation over Alaskan North Slope tundra.

In general, we use  $NSE$  to evaluate the model’s performance in capturing seasonality (i.e., time series) of  $CH_4$  and  $CO_2$  net fluxes and optimize  $CH_4$  and  $CO_2$  simulations. We use  $RMSE$  and  $MAE$  to assess the model’s capability in simulating the magnitudes of soil temperature, moisture saturation,  $ZCP$  durations, and cumulative  $CH_4$  and  $CO_2$  emissions.

## 4 Results and Discussion

### 4.1 Evaluation of Soil Temperature and Zero-curtain Period

We first evaluated the simulated daily soil temperature profiles against the observations from ABoVE and GIPL-UAF at the four site locations. Then, we examined improvements in simulations of soil temperature, soil moisture, and the durations of ZCPs by employing the newly revised phase-change scheme (i.e., “NewPC\_OriDecomOriCH4”; Table 2).

Results for the BES/CMDL and IVO site are shown in Figure 2; results for other sites are shown in supplementary Figure S4. At BES/CMDL, the baseline (i.e., “OriPC\_OriDecomOriCH4”; Table 2) simulated soil temperatures ( $T_s$ ) with the default phase-change scheme ( $T_s$ \_OriPC; blue lines; Figure 2a) decrease rapidly in fall due to the overestimated freezing rate (i.e., the slope of decreasing liquid water fraction), notably underestimating the duration of the ZCP (bluish shaded area). Consequently, liquid water saturation ( $S_f$ \_OriPC, green lines; Figure 2a) quickly drops to a lower bound (i.e., the supercooled liquid water content divided by porosity), and the freezing process generally completes within a short period (days for top layers to one month at the most for deeper layers). The baseline model soil temperature drops ( $T_s$ \_OriPC) sharply after the freezing process ends (i.e.,  $S_f$ \_OriPC decreases to the lower bound). In contrast, the new phase-change scheme effectively slows freezing rates, showing relatively smaller slopes of decreasing liquid water saturation ( $S_f$ \_NewPC; magenta lines; Figure 2a) within the ZCPs than the baseline simulation ( $S_f$ \_OriPC; green lines) especially in the 4<sup>th</sup> and 5<sup>th</sup> layer. Hence, the gradually released latent heat maintains soil temperatures around the freezing point for a longer period ( $T_s$ \_NewPC; red lines; Figure 2a), effectively extending the ZCPs (reddish shaded area) which agree better with observations (grey shaded area) than the baseline results. The ZCP duration increases with depth and can extend into December for deep soil layers. Similarly, improved performance was found at the BEO and ATQ sites (supplementary Figure S4). At IVO, however, while the new phase-change scheme greatly improved simulated results relative to the baseline simulation (Figure 2b), the model still slightly underestimated ZCP durations and also underestimated winter (December to April) soil temperature (red vs. black). This result at IVO is consistent with the underestimation of late-season soil liquid water available to be frozen, and thereby to release sufficient latent heat (Figure S5). In general, the improvements in ZCP are larger in deeper layers than topsoils, with the top layer showing only marginal improvement.

Simulated ZCP durations with the revised phase-change scheme (NewPC) demonstrated notable improvements over the baseline (original) phase-change scheme (OriPC) (solid circles vs. open diamonds) (Figure 3), showing greatly reduced mean absolute errors (MAEs) (Table 3). For example, at 12 cm depth (4<sup>th</sup> layer), the relative improvements in MAE of the ZCP durations were 65%, 65%, 66%, and 50% for the four site locations (Table 3). The largest improvement in MAE was as large as 65 days for the 6<sup>th</sup> layer at BES/CMDL, with a relative improvement of 84% (Table 3). This large improvement stems from the better-estimated ALT at this site; the OriPC simulated 6<sup>th</sup> layer temperature remained below freezing, leading to a zero-day ZCP (diamonds on the x-axis in Figure 3). The new phase-change scheme not only improved simulation of the ZCP and

cold-season soil temperatures, but also affected the warm season dynamics and thus ALT estimates. As Figure 3 indicates, the  
375 NewPC improved simulated ALTs at all four site locations with reduced bias in multi-year averaged ALT, resulting in more  
reasonable ZCP durations for the 6<sup>th</sup> layer (and also the 7<sup>th</sup> layer for IVO), while the baseline results were zero days.

The deeper active layer simulated by NewPC implies more soil water storage capacity, resulting in lower soil moisture in  
shallow soil layers and higher soil water in deep layers ( $S_{f\_NewPC}$ ; magenta lines; Figure 2) compared to baseline results.  
380 The changes in soil liquid water content, in turn, impact phase-change and soil temperature simulations. Comparison with the  
observed soil liquid water content reveals a better agreement with observations (Table S5). For example, at ATQ (Figure S7),  
the RMSEs of the liquid water content were reduced by 5.4%, 35.3%, 42.6%, and 25.4% for the 3<sup>rd</sup> through 6<sup>th</sup> layers,  
respectively (Table S5).

385 The changes to model representations of phase change led to large reductions in soil temperature bias. The relative  
improvements in RMSE of simulated soil temperatures during Sep. and Oct. (i.e., the two months that the ZCPs usually cover),  
generally increased with depth for surface layers (within about 20 cm of the surface, i.e., 1<sup>st</sup> to 4<sup>th</sup> layer), and were above 80%  
for the intermediate layers (5<sup>th</sup> to 8<sup>th</sup>) at all the sites (Figure 4). At the two Barrow sites where observed soil temperatures were  
available, the relative improvements for the deepest (13<sup>th</sup>) layer were 72.6% and 71.1%, on average, for the early winter and  
390 annual cycle, respectively. Therefore, incorporating the new phase-change scheme also resulted in improved bottom  
temperature boundary conditions, which is critical for accurately simulating permafrost dynamics (Sapriza-Azuri et al., 2018).  
Improvements between September and December and the whole annual cycle also increased with soil depth, showing site-  
averaged reductions in RMSEs ranging from 47% to 63% and from 36% to 46% for the two periods, respectively. The whole  
cold-season period (Sep. to May) showed, on average, 44% to 53% reduction in RMSEs from the 1<sup>st</sup> to 6<sup>th</sup> layer at relatively  
395 warmer sites (i.e., ATQ and IVO), and from 19% to 69% for the top 13 layers for the two Barrow sites.

Soil temperatures were still slightly underestimated during the thawing season (i.e., May) at all four sites, showing later onset  
of thawing indicated by the timing when warming soil temperatures cross 0°C and soil moisture starts to rise (Figure 2). One  
possible reason for this bias is the lack of representation of advective heat transport. That is, the model does not represent the  
400 heat of spring rain that is advectively transported into soils (Neumann et al., 2019; Mekonnen et al., 2020); nor does it account  
for advective heat transport associated with water fluxes in subsurface soils after the spring-rainwater mix with existing cold  
liquid water in soils. Also, after the freezing process ends, simulated deeper soil layer temperatures were underestimated (e.g.,  
December through April). This bias might be caused by underestimated snow depth (Figure S9) resulting from inaccurate  
forcing (particularly snowfall), land cover, microtopography, and/or wind-blown snow redistribution.

405

The improved simulations of soil temperature, liquid water content, and ZCP duration greatly impacted soil HR and methane  
production but did not necessarily guarantee improvements in CO<sub>2</sub> and CH<sub>4</sub> emissions. In the next section, we closely evaluate

simulated CH<sub>4</sub> and CO<sub>2</sub> fluxes with different parameterizations of environmental modifiers and the modified CH<sub>4</sub> parameterizations as described in Section 3.1.

410

## 4.2 Evaluation of CO<sub>2</sub> and CH<sub>4</sub> Fluxes

Here we evaluate the simulated monthly CO<sub>2</sub> and CH<sub>4</sub> fluxes at the site scale against EC tower observations. Figure 5 displays the NSEs of ELMv1-ECA simulations using different carbon decomposition schemes and CH<sub>4</sub> process-related parameters, i.e., “NewPC\_NewDecomNewCH<sub>4</sub>” (grey dots) (see configurations in Table 2). (Time series of all the simulations are provided in Figure S7). The failure of simulated CH<sub>4</sub> emissions to capture the methane seasonality at IVO (as indicated by Figure S8) might occur because of the lack of 1) a reasonable wetland module that can adequately account for inundated hydro-ecological dynamics, 2) advective heat transport at the air-ground interface through rainfall infiltration and within subsurface soils through water transfer, and 3) the geological micro-seepage emission of CH<sub>4</sub>, as reported in previous studies (Anthony et al., 2012; Etiope and Klusman, 2010; Russell et al., 2020). For instance, Lyman et al. (2020) showed large temporal variability of CH<sub>4</sub> at natural gas well pad soils, similar to the observations at IVO (Anthony et al., 2012). The advective heat transport not only impacts soil temperature, but also affects soil moisture redistribution, substrate availability, and microbial activity; this mechanism and wetland inundation dynamics together would cause hysteretic effects on CH<sub>4</sub> emission response to soil temperatures (Chang et al., 2020; 2021). In the future, we will apply a Macromolecular Rate Theory (MMRT)-based temperature sensitivity approach (Chang et al., 2020; 2021) to address the hysteresis effect on CH<sub>4</sub> emissions and explore more on the contribution of geological micro-seepage emission. The three mechanisms discussed above (i.e., wetland dynamics, advective heat transport, and geological micro-seepage CH<sub>4</sub> emission) currently missing in our model are likely necessary to simulate CH<sub>4</sub> emissions at this site, and we therefore do not include CH<sub>4</sub> analysis at IVO in the following sections.

The improved phase-change scheme, and thus improved simulations of ZCP durations and soil temperature and moisture, resulted in greatly improved performance for CO<sub>2</sub> emissions at BES/CMDL and BEO, and slightly better performance for CH<sub>4</sub> emissions at ATQ, compared to the baseline (blue for “NewPC\_OriDecomOriCH<sub>4</sub>” vs. green for baseline; Figure 5), even though the carbon decomposition and methane model remained the same as the baseline. Incorporating the revised CH<sub>4</sub> model with the default parameter (discussed in section 3.1.3) improved simulated CH<sub>4</sub> emissions at BES/CMDL, BEO, and ATQ (magenta for “NewPC\_OriDecomNewCH<sub>4</sub>” vs. blue for “NewPC\_OriDecomOriCH<sub>4</sub>”), especially during the cold season (Figure S8). The improved NSEs for CH<sub>4</sub> emissions mainly resulted from increased emissions over early winter (Sep. and Oct.) and slight but persistent enhancements throughout the rest of the cold season (magenta in Figure S8), which were related to our modifications to CH<sub>4</sub> transport mechanisms. Further, with the identified optimal parameterization of environmental modifiers to the base decomposition rate and methane parameters, results demonstrate substantial improvements to the simulation of CO<sub>2</sub> net flux and CH<sub>4</sub> emissions compared to baseline results (red vs. others; i.e., shortest distance from ( $NSE_{CH_4}$ ,  $NSE_{CO_2}$ ) to (1, 1)). Among the 121 common schemes providing good performance for both CO<sub>2</sub> and CH<sub>4</sub> emissions (i.e., both

440

$NSE_{CH_4}$  and  $NSE_{CO_2}$  larger than 0.5, indicated by the grey dots within the boxes in Figure 5), we identified a generic scheme by selecting the common parameterization that provided the best overall performance for all the sites (except IVO) (cyan; Figure 5). The specific environmental modifier functions and methane parameters for the optimal and generic scheme are provided in Table S6.

445

Figure 6 illustrates the uncertainty associated with the model representations of environmental influences on heterotrophic respiration and methane parameters. The optimal simulations at the study sites either used the modified ELMv1-ECA moisture scalar or Yanetal (see Table S6), i.e., two groups of moisture-dependency functions implemented for each soil layer. For the Sierra et al. (2015) empirical moisture functions, the influence of liquid moisture content on heterotrophic respiration is uniformly applied to all active soil layers, even though the soil properties (e.g., porosity and saturated soil water potential) are quite different vertically. ELMv1-ECA's moisture scalars (including the original scheme) that use soil water potential, in contrast, reasonably explained the varying influence along with the vertical soil profile (Niu and Yang, 2006). The Yanetal moisture functions also used soil layer-dependent porosity and clay content to calculate relevant parameters (Yan et al., 2018). The simulations with moisture functions documented in Sierra et al. (2015) generally overestimated  $CO_2$  and  $CH_4$  emissions, especially during the warm season when the thaw depth is deep and soil wetness is high, thus permitting large moisture modifier scalar applied to the base decomposition rates for all the soil layers regardless of soil properties.

Reducing the minimum soil water potential  $\psi_{min}$  for moisture scalar effectively prevents the possibility of zero respiration in subfreezing soils during wintertime (Figure 6). This change exerts more impact on cold sites, such as the two Barrow sites, due to the smaller supercooled liquid water under the colder temperature. Thus, the improved NSEs for  $CO_2$  and  $CH_4$  emissions at BES/CMDL and BEO were larger than those at ATQ (Figure 5). Since the temperature at ATQ was not cold enough to make the supercooled liquid water content small enough to give a zero moisture scalar, the microbial respiration was not completely shut down with the original decomposition modifier at this site. Indeed, at ATQ, where cold-season temperatures are relatively warmer than at BES/CMDL and BEO, simulations with the original ELMv1-ECA environmental modifier (i.e., "NewPC\_OriDecomNewCH4" in Figure S8; discussed in Section 3.1.2), already released much more  $CO_2$  and  $CH_4$  throughout the cold season than in the baseline simulations, owing to the improved simulations of soil temperature and moisture, and the modifications for  $CH_4$  transport.

The optimal simulations used Daycent2 temperature-dependency function at ATQ and  $Q_{10}$ -based temperature functions at BES/CMDL and BEO with high  $Q_{10}$  values (e.g., 2.0 and 2.5, respectively) (Table S6), mutually mediating the response of microbial respiration with moisture functions discussed above. At all three sites, the optimized parameterizations used a higher  $\epsilon_{aere}$  (i.e., 0.05; Table S6), representing possible cold-season  $CH_4$  emissions through ice cracks and remnants of aerenchyma tissues. This newly introduced variable is highly uncertain, though; it can be calibrated at any other sites against cold-season measurements. At BES/CMDL, the optimized parameterization used a decreased maximum  $CH_4$  oxidation rate constant which

475 has been reported highly uncertain, especially over high latitudes (Riley et al., 2011). The generic scheme overlaps with the optimized parameterization at BES/CMDL, which provided the best overall performance at all three sites (Table S6). Despite the small site number and the limited spatial representativeness of each site, the identified generic decomposition scheme might be applied to the Alaska North Slope tundra. Nevertheless, the generic decomposition scheme might induce uncertainty in simulations and might not be the optimal regional scheme over other ecosystems or given different climate forcing and soil  
480 conditions. Still, we conclude that when using ELMv1-ECA, the generic decomposition scheme can serve as a reasonable initial scheme for estimating CO<sub>2</sub> and CH<sub>4</sub> emissions over other high-latitude areas (e.g., Figure S10). In the future, we will explore more sites from newly published CO<sub>2</sub> and CH<sub>4</sub> datasets from pan-Arctic ecosystems, e.g., BAWLD-CH<sub>4</sub> (Kuhn et al., 2021) and FLUXNET-CH<sub>4</sub> (Delwiche et al., 2021; Knox et al., 2019).

485 The extended ZCPs, the revised environmental modifier to decomposition, and the modified CH<sub>4</sub> transport mechanism and oxidation parameter together resulted in large improvements for both CO<sub>2</sub> and CH<sub>4</sub> emissions, especially over the cold season. Nevertheless, the optimal simulations still overestimated the contribution of the early cold season (Sep. and Oct.) CO<sub>2</sub> emissions at BEO and ATQ (top panel; Figure 7), and underestimated CH<sub>4</sub> emissions during post-ZCP months (e.g., Oct. to Dec.) (bottom panel; Figure 7). Many reasons are responsible for the early cold-season CO<sub>2</sub> overestimations, including model  
490 deficiencies, prescribed land parameters, and possibly inaccurate forcing. As for the underestimations of post-ZCP carbon emissions, one critical reason is the lack of sudden bursts of CO<sub>2</sub> and CH<sub>4</sub> within the model, i.e., the gases are pushed out of freezing soils during the freeze-up period (Mastepanov et al., 2008; Pirk et al., 2017). Currently, the ELMv1-ECA mimics this sudden burst mechanism by preventing CO<sub>2</sub> and CH<sub>4</sub> from dissolving in the soil ice fraction (Riley et al., 2011), which could capture some burst emissions (e.g., CH<sub>4</sub> emissions in Oct. and Sep. of 2013 at ATQ; Figure 6); but it still shows an overall  
495 underestimation for sudden-burst emissions especially at colder sites (e.g., BES/CMDL and BEO; Figures 6 and 7). We will improve this mechanism in the future by explicitly simulating ice encroaching soil pores and pushing out gases and liquid water out of the soil matrix. In the next section, we quantify the cold season contribution of CO<sub>2</sub> and CH<sub>4</sub> emissions and then estimate the historical trends of seasonal CO<sub>2</sub> and CH<sub>4</sub> emissions from 1950 to 2017.

### 500 **4.3 Cold-season Contribution of CH<sub>4</sub> and CO<sub>2</sub> emissions and Historical Trends**

Throughout this section, we only retain and discuss the identified optimal simulation results (i.e., ELM\_NewPC\_Optimized) for each site. To better verify the cold-season contribution of CH<sub>4</sub> and CO<sub>2</sub> emissions to the annual budget, a multi-year average approach was taken because of discontinuity in the observed time series.

505 The new simulation results with the optimal parameterization showed greatly enhanced performance in terms of capturing the averaged seasonal cycle (red; Figure 7), especially for the cold-season months (Sep. to May; Figure 7), reducing site-averaged MAEs in cold-season total CH<sub>4</sub> and CO<sub>2</sub> emissions by 72% and 70% (Figure 8, Table 4), respectively. Specifically, compared

to baseline results which significantly underestimated the cold-season carbon emissions, the optimized simulation results showed 0.79 gC m<sup>-2</sup> and 44.0 gC m<sup>-2</sup> increases in site-averaged cold-season CH<sub>4</sub> and CO<sub>2</sub> emissions, respectively. The optimized simulations reduced biases in early cold-season (cold-season) CH<sub>4</sub> emissions by 80% (74%), 86% (76%), and 77% (61%) for BES/CMDL, BEO, and ATQ (Table 4), respectively. The observed cold-season CH<sub>4</sub> emissions contributed at least ~40% to the annual total at three of the study sites, of which about half occurred in early cold-season months (Sep. and Oct.) (Figure 8, Table 4), i.e., the two months hosting the major part of ZCPs for the top to intermediate soil layers. The simulated contributions of early cold-season (Sep. and Oct.) CH<sub>4</sub> emissions to the cold-season total were 51%, 65%, and 55% for the three sites, in comparison with the observed 47%, 58%, and 43%, showing slight overestimations. Compared to the baseline-simulated percentage of cold-season contributions to the annual total CH<sub>4</sub> emissions (i.e., only 5%, 6%, and 15%), the optimized simulation showed greatly improved agreements with observed contributions, i.e., 35%, 35%, 33% vs. 45%, 42%, 45% for BES/CMDL, BEO, and ATQ, respectively.

The optimized simulations showed larger improvements in cold-season CO<sub>2</sub> emissions (Figure 8, Table 4) for cold sites (i.e., BES/CMDL and BEO) than for the warmer site (i.e., ATQ and IVO). Specifically, compared to baseline results, the updated ELMv1-ECA reduced the biases in simulated cold-season CO<sub>2</sub> emissions from -56.1 gC m<sup>-2</sup> (64% of the observation) to -12.1 gC m<sup>-2</sup> (14% of the observation) for BES/CMDL and from -65.0 gC m<sup>-2</sup> (68% of the observation) to -12.4 gC m<sup>-2</sup> (13% of the observation) for BEO. In contrast, the optimized simulation showed slight overestimations for cold-season CO<sub>2</sub> emissions at ATQ and IVO (Table 4). Nevertheless, the optimized ELMv1-ECA provided greatly improved warm-season CO<sub>2</sub> net flux for all the four sites, reducing biases by 110%, 78%, 37%, and 102% compared to baseline results at BES/CMDL, BEO, ATQ, and IVO, respectively. Indeed, the updated model switched warm-season net CO<sub>2</sub> flux from baseline-simulated net emissions (positive CO<sub>2</sub> net flux) to net uptake (negative CO<sub>2</sub> net flux) at BES/CMDL, BEO, and IVO, correctly matching with observed warm-season CO<sub>2</sub> net flux (Figure 8).

The observed multi-year averaged annual CO<sub>2</sub> net flux was 19.9 gC m<sup>-2</sup> (source), 31.8 gC m<sup>-2</sup> (source), -3.8 gC m<sup>-2</sup> (sink), and -16.7 gC m<sup>-2</sup> (sink) at BES/CMDL, BEO, ATQ, and IVO, respectively. However, due to the large discontinuity in CO<sub>2</sub> observations (Figure 6), the calculated annual CO<sub>2</sub> budget is uncertain. Still, we can characterize the CO<sub>2</sub> budget with simulated results using the updated ELMv1-ECA. We find that the simulated cold-season CO<sub>2</sub> emissions were larger than the warm-season CO<sub>2</sub> net uptake during the analysing period (2013-2017) at all four sites (Figure 8), showing annual CO<sub>2</sub> net flux as 1.1 gC m<sup>-2</sup> (source), 36.6 gC m<sup>-2</sup> (source), 36.5 gC m<sup>-2</sup> (source), and 18.2 gC m<sup>-2</sup> (source) at BES/CMDL, BEO, ATQ, and IVO, respectively. The simulated CO<sub>2</sub> emissions over the early cold season (Sep. and Oct.) accounted for 50%, 56%, 66%, and 35% of the total emissions throughout the cold season for BES/CMDL, BEO, ATQ, and IVO, respectively.

Through trend analysis between 1950 and 2017, we found that the ZCP durations showed increasing trends at all three sites, with ZCP trends increasing with depth (Table 5). At ATQ, a warmer site than BES/CMDL and BEO, the trends of ZCP

545 durations increase from 0.12 to 0.49 days yr<sup>-1</sup> along with the vertical soil profile. At BES/CMDL and BEO, only soil layers at 3 cm and 6 cm show statistically significant increasing trends, ranging from 0.10 to 0.13 days yr<sup>-1</sup>. The CO<sub>2</sub> emissions during the 6 cm ZCP and during cold-season months (September to May) both showed increasing trends at all three sites (Table 6), ranging from 0.12 to 0.17 gC m<sup>-2</sup> yr<sup>-1</sup> for the 6 cm ZCP, and from 0.30 to 0.40 gC m<sup>-2</sup> yr<sup>-1</sup> for the entire cold season period. Annual CH<sub>4</sub> emissions showed a nonsignificant increasing trend at ATQ with a rate of 0.52 mgC m<sup>-2</sup> yr<sup>-1</sup>; but neither annual nor cold-season CH<sub>4</sub> emissions show increasing trends at other sites. In the future, we will examine the generic model parameterization at more sites over the pan-Arctic; we will also optimize regional simulations against spatial datasets of CO<sub>2</sub> and CH<sub>4</sub> upscaled from in-situ measurements over pan-Arctic permafrost domain (Natali et al., 2019; Virkkala et al., 2021; Zeng et al., 2020; Peltola et al., 2019), and discuss the uncertainty of estimated trends of the spatially averaged CO<sub>2</sub> and CH<sub>4</sub> emissions associated with snow impact and model parameterizations.

## 5 Summary and Discussion

555 In this study, we improved ELMv1-ECA simulated subsurface soil temperature, zero-curtain period durations, and cold-season CH<sub>4</sub> and CO<sub>2</sub> net emissions at Alaskan North Slope tundra sites. We first improved the numerical representation of coupled water and heat transport with freeze-thaw processes via modifying ELMv1-ECA's phase-change scheme. Then, we revised the dependency of soil decomposition rates on soil temperature and moisture. We further refined the cold-season methane processes by mimicking emission pathways through ice cracks and remnants of aerenchyma tissues, reducing the maximum oxidation rate constant, and reducing upper boundary (snow) resistance that allows CH<sub>4</sub> to be emitted from frozen soils through snow to the atmosphere. We also used the updated ELMv1-ECA to estimate historical trends of cold-season CH<sub>4</sub> and CO<sub>2</sub> net emissions at the Alaskan tundra sites from 1950 to 2017. This study is among the first efforts toward improving simulations of zero-curtain periods and cold-season carbon emissions over the Arctic tundra by ESMs. The strategy of improving ELMv1-ECA phase-change scheme, environmental controls on microbial activity, and methane parameterizations can be easily applied to other global land models.

565 With the revised phase-change scheme, the updated ELMv1-ECA greatly improved site-scale simulations of soil temperature, soil moisture, and zero-curtain period. Specifically, the RMSE of daily subsurface soil temperature was substantially reduced compared to the baseline simulation, showing site-averaged improvements ranging from 58% to 87% over the early cold season (Sep. to Oct.) and from 36% to 46% over the annual cycle for soil layers within the active layer. The evaluation of simulated liquid water content with the new phase-change scheme, although limited by the availability of observations, showed a relative reduction in RMSE as high as 43% for the 5<sup>th</sup> layer at ATQ, and site-averaged improvements of 15% and 21% for the 4<sup>th</sup> and 5<sup>th</sup> layer, respectively. Simulated ZCP durations were also greatly improved, with, e.g., relative reductions in MAEs of 65%, 65%, 66%, and 50% for the 4<sup>th</sup> layer (about 12 cm) at BES/CMDL, BEO, ATQ, and IVO, respectively.

Based upon the improved simulations of soil temperature and moisture with the new phase-change scheme, the identified  
575 optimal SOC decomposition scheme, and the revised methane module, the site-averaged mean annual errors of cold-  
season emissions were reduced by 72% and 70% for CH<sub>4</sub> and CO<sub>2</sub>, respectively. We also found that CH<sub>4</sub> and CO<sub>2</sub> emissions  
over the early cold season, i.e., September and October, which usually account for most of the zero-curtain period, contributed  
more than 50% of the total emissions throughout the cold season (September to May). Zero-curtain period durations showed  
increasing trends from 1950 to 2017, with larger trends in deeper soil layers. Also, both CO<sub>2</sub> emissions during the 6 cm depth  
580 zero-curtain period and the entire cold-season period (Sep. to May) showed increasing trends.

Although showing improvements compared to baseline results, the new simulations generally overestimated the contribution  
of the early cold season (Sep. and Oct.) CO<sub>2</sub> emissions at BEO and ATQ. Many reasons could contribute to the overestimations,  
including poor representation of coupled biogeochemical and hydrological processes in the localized permafrost soil  
585 environment, the lack of accurate representation of inundated hydro-ecological dynamics, underestimation of snow  
accumulation due to micro-topographic effects, and thus the snow insulation to the ground (e.g., Bisht et al., 2018), among  
others. Strong microtopographic impacts on CO<sub>2</sub> and CH<sub>4</sub> emissions across seven landscape types in Barrow, Alaska, were  
recently reported (Wang et al. (2019); Grant et al., 2017a; Grant et al., 2017b). Sensitivity analysis demonstrates large impacts  
of snow depth on simulated winter soil temperature, summer soil moisture, heterotrophic respiration, and CO<sub>2</sub> fluxes (Figure  
590 S9). The underestimated emissions during post-ZCP months (Oct. to Nov.) are mainly caused by the lack of sudden bursts of  
CO<sub>2</sub> and CH<sub>4</sub> during the freeze-up period. In addition, the single static multiplicative function used to parameterize the impact  
of environmental conditions on respiration might not be appropriate because the environmental impact also depends on  
maximum respiration rate, soil texture, soil carbon content and quality, and microbial biomass (Tang and Riley, 2019).  
Moreover, due to lacking representations of wetland hydro-ecological dynamics, the model uses simulated upland  
595 heterotrophic respiration to estimate CH<sub>4</sub> production (Riley et al., 2011), which might cause underestimations of CH<sub>4</sub>  
emissions, especially under wet conditions. Also, inappropriately prescribed land cover at the site scale or inaccurate climate  
forcing (particularly air temperature and precipitation; Chang et al. (2019)) could all impact snow accumulation processes (Tao  
et al., 2017), which can significantly impact CO<sub>2</sub> and CH<sub>4</sub> emission simulations. Customizing the complex local ecosystem  
vegetation community might be feasible at the site scale, however, it is less possible for regional or global land model  
600 simulations. This issue calls for the importance of upscaling methods to model (e.g., Pau et al., 2016; Liu et al., 2016) and  
measure (e.g., Natali et al., 2019; Virkkala et al., 2019) carbon and water cycle dynamics at the regional and global scales.

Given the persistent warming and the continued more severe warming in the cold season (Box et al., 2019), we envision  
continuing increases in cold-season CO<sub>2</sub> and CH<sub>4</sub> emissions from the permafrost tundra ecosystem. The increasing rate of  
605 cold-season heterotrophic respiration (releasing CO<sub>2</sub>) may become larger than the trend of warm-season vegetation CO<sub>2</sub> uptake  
under future climate. To accurately characterize cold-season emissions and warm-season net uptake, models have to correctly  
simulate both components, which, however, few models can do. The updated ELMv1-ECA, with the enhanced capacity to

reproduce cold-season CO<sub>2</sub> and CH<sub>4</sub> emissions proven by this study, can serve as a starting point to better predict permafrost carbon responses to future climate. Finally, the complex water-carbon interactions require modeling systems with fully coupled hydrological-thermal-biogeochemical processes to better predict the carbon budget in permafrost regions under future climate.

### **Code/Data availability**

The observations used in this study are available at <http://dx.doi.org/10.3334/ornl daac/1300> and <https://doi.org/10.3334/ornl daac/1562>. The UAF observations are available at <http://permafrost.gi.alaska.edu>. The updated version of ELMv1-ECA will be available at GitHub (<https://github.com/jingtao-lbl/E3SM>).

### **615 Author contributions**

JT assembled observations, developed the methodology, conducted model simulations, analysed results, and wrote and revised the paper. QZ and WJR contributed to experiment design, editing the original and revised manuscript. RBN edited the original and revised manuscript, and provided valuable discussion and guidance.

### **Competing interests**

620 The authors declare that they have no conflict of interest.

### **Acknowledgments**

We are grateful for valuable discussions with Jinyun Tang, Roisin Commane, Xiyan Xu, Kai Yang, and Chenghai Wang. We thank the anonymous reviewers for their helpful comments. This material is based upon work supported by the U.S. Department of Energy, Office of Science, Office of Biological and Environmental Research under Award Number DE-625 SC0019063.

## Appendices: Description of Relevant Modules within ELMv1-ECA

Here we describe the heat transfer in subsurface soils, the carbon decomposition, and the methane module within the ELMv1-ECA that are of particular relevance to our study.

### 630 Appendix A Subsurface Heat Transfer

ELMv1-ECA approximates the subsurface heat transfer process with a one-dimensional heat diffusion equation:

$$c \frac{\partial T}{\partial t} = \frac{\partial}{\partial z} \left( \lambda \frac{\partial T}{\partial z} \right), \quad (\text{Eq. A1})$$

where  $T$  is the soil temperature (K),  $c$  is the volumetric soil heat capacity ( $\text{J m}^{-3} \text{K}^{-1}$ ),  $\lambda$  is soil thermal conductivity ( $\text{W m}^{-1} \text{K}^{-1}$ ), and  $z$  is the soil depth (m) of the ELMv1-ECA soil layers. The ELMv1-ECA soil column consists of 15 layers, with soil thickness increasing exponentially with depth. The bottom of soil column is down to 42 m, and the top 10 layers are hydrologically active with layer node depth as 0.0071 m, 0.0279 m, 0.0623 m, 0.1189 m, 0.2122 m, 0.3661 m, 0.6198 m, 1.0380 m, 1.7276 m, 2.8646 m, respectively. The soil heat capacity and thermal conductivity is updated at each time step based on the fractions of soil matrix components, i.e., liquid water content, ice content, and soil solids. The impact of organic carbon on soil thermal and hydraulic properties was incorporated as a linear combination of the counterparts properties of mineral soil and organic matter (Lawrence and Slater, 2008). To solve the (Eq. A1), ELMv1-ECA employs the Crank-Nicholson method, resulting in a tridiagonal system equation. We assume a zero-flux bottom boundary condition. The top boundary condition is estimated by solving the energy balance equation at the air and ground interface, with additionally an overlying five-layer snow model and a one-layer surface water model in between. When snow and surface water present, ELMv1-ECA incorporates the snow layers and surface water layer into the tridiagonal system to solve the heat transfer along the entire column.

645 ELMv1-ECA incorporates freeze-thaw processes of soil water in a decoupled way. Specifically, the model determines the onset of melting or freezing by soil temperature initially solved at time step  $n + 1$  without consideration of the phase change process, denoted as  $T_i^{n+1}$ , i.e.,

$$\begin{aligned} T_i^{n+1} > T_f \text{ and } w_{ice,i}^n > 0 & \quad \text{melting} \\ T_i^{n+1} < T_f \text{ and } w_{liq,i}^n > w_{liq,max,i}^{n+1} & \quad \text{freezing} \end{aligned}, \quad (\text{Eq. A2})$$

where  $T_f$  is the freezing temperature of water ( $0^\circ\text{C}$  in Kelvin, i.e., 273.15 K),  $w_{ice,i}^n$  and  $w_{liq,i}^n$  is the mass of ice and liquid water ( $\text{kg m}^{-2}$ ) of layer  $i$ , and  $w_{liq,max,i}^{n+1}$  ( $\text{kg m}^{-2}$ ) is the supercooled liquid water that is allowed to coexist with ice given the subfreezing soil temperature  $T_i^{n+1}$ . This  $w_{liq,max,i}^{n+1}$  varies with soil texture and temperature and is calculated by the freezing point depression equation (Niu and Yang, 2006),

$$w_{liq,max,i}^{n+1} = \Delta z_i \theta_{sat,i} \left[ \frac{10^3 L_f (T_f - T_i^{n+1})}{g T_i^{n+1} \psi_{sat,i}} \right]^{-1/B_i}, \quad (\text{Eq. A3})$$

where  $\Delta z_i$  is the soil thickness of the  $i$ th layer (in mm),  $\theta_{sat,i}$  represents the soil porosity (i.e., the saturated volumetric water content),  $L_f$  is the latent heat of fusion ( $\text{J kg}^{-1}$ ),  $B_i$  is the Clapp and Hornberger exponent (Clapp and Hornberger, 1978),  $g$  is the gravitational acceleration ( $\text{m s}^{-2}$ ), and  $\psi_{sat,i}$  is the soil texture-dependent saturated matric potential (mm).

655

The rate of phase change is initially assessed from the heat excess (or deficit) needed to change the estimated temperature to the freezing point. Specifically, the model first computes the energy ( $H_i$ ) needed for adjusting current soil temperature ( $T_i^{n+1}$ ) to  $T_f$ :

$$\begin{aligned} H_i &= -c_i \frac{\Delta z_i}{\Delta t} T_{inc} + (1 - f_{sno} - f_{h2osfc}) \frac{\partial h}{\partial T} T_{inc} & i = 1 \\ H_i &= -c_i \frac{\Delta z_i}{\Delta t} T_{inc} & i > 1 \end{aligned}, \quad (\text{Eq. A4})$$

where  $T_{inc} = T_f - T_i^{n+1}$ ,  $h$  is ground heat flux,  $f_{sno}$  and  $f_{h2osfc}$  is the snow and surface water fraction within the grid cell, respectively. The mass change involved then is computed as  $H_m = \frac{H_i \Delta t}{L_f}$  (i.e.,  $-c_i \frac{\Delta z_i}{L_f} T_{inc}$  for soils below the top interface layer). That is, the mass of ice increased/decreased by freezing/melting is  $-H_m$ , releasing/absorbing energy  $H_i$  to bring up/down the current soil temperature to  $T_f$ . Accordingly, the ice and liquid mass are adjusted as:

660

$$\begin{aligned} w_{ice,i}^{n+1} &= \begin{cases} \min(w_{ice,i}^n + w_{liq,i}^n - w_{liq,max,i}^{n+1*}, w_{ice,i}^n - H_m) & w_{liq,i}^n + w_{ice,i}^n \geq w_{liq,max,i}^{n+1*} \\ 0 & w_{liq,i}^n + w_{ice,i}^n < w_{liq,max,i}^{n+1*} \end{cases} \\ w_{liq,i}^{n+1} &= \max(w_{liq,i}^n + w_{ice,i}^n - w_{ice,i}^{n+1}, 0) \end{aligned}. \quad (\text{Eq. A5})$$

The  $H_i$  then is adjusted to  $H_i^*$ , calculated as  $H_i^* = H_i - \frac{L_f(w_{ice,i}^n - w_{ice,i}^{n+1})}{\Delta t}$ . The  $H_i^*$  then is the ultimately determined latent heat and is used to further readjust soil temperature as in equation (Eq. A6),

$$T_i^{n+1*} = T_f + \frac{\Delta t}{c_i \Delta z_i} H_i^* = T_f - \frac{L_f(w_{ice,i}^n - w_{ice,i}^{n+1})}{c_i \Delta z_i}, \quad (\text{Eq. A6})$$

665 in which the temperature adjusted to  $T_f$  is further increased by  $-\frac{L_f(w_{ice,i}^n - w_{ice,i}^{n+1})}{c_i \Delta z_i}$  due to soil freezing since  $w_{ice,i}^{n+1} \geq w_{ice,i}^n$ , or decreased due to melting when  $w_{ice,i}^{n+1} < w_{ice,i}^n$ .

Incorporating soil-water freezing phase change into equation (Eq. A1), we can rewrite the heat (conduction) transfer equation as (Eq. A7) or (Eq. A8),

$$c \frac{\partial T}{\partial t} = \frac{\partial}{\partial z} \left( \lambda \frac{\partial T}{\partial z} \right) - L_f \rho_{liq} \frac{\partial \theta_{liq}}{\partial t}, \quad (\text{Eq. A7})$$

$$\left( c + L_f \rho_{liq} \frac{\partial \theta_{liq}}{\partial T} \right) \frac{\partial T}{\partial t} = \frac{\partial}{\partial z} \left( \lambda \frac{\partial T}{\partial z} \right), \quad (\text{Eq. A8})$$

670 where  $L_f$  is the latent heat of fusion ( $\text{J kg}^{-1}$ ),  $\theta_{liq}$  is soil liquid water content ( $\text{m}^3 \text{m}^{-3}$ ), and  $\rho_{liq}$  is the density of liquid water ( $\text{kg m}^{-3}$ ). To solve (Eq. A8), we need to compute the derivative of the soil freezing characteristic curve ( $\theta_{liq}(T)$ ) with respect to temperature ( $\frac{\partial \theta_{liq}}{\partial T}$ ). As discussed above, we approximate the  $\theta_{liq}(T)$  curve by combining the freezing point temperature-depression equation (Fuchs et al., 1978) and the soil water retention curve (Clapp and Hornberger, 1978). This leads to the supercooled water formulation (Eq. A3) (Niu and Yang, 2006). Computing  $\frac{\partial \theta_{liq}}{\partial T}$  requests the soil freezing curves  $\theta_{liq}(T)$  to be

675 continuous and differentiable for a range of temperatures during the freezing process (Kurylyk and Watanabe, 2013; Hansson et al., 2004). Here, we follow the existing ELM framework discussed above to solve (Eq. A8). The original numerical representation for readjusting soil temperature (Eq. A6) obtained by the uncoupled two-step implementation (Eq. A2 to A5) significantly overestimates soil water freezing rates. Two reasons are responsible for the overestimation. First, the freezing point ( $T_f = 0^\circ\text{C}$ ) is used to determine the occurrence of soil water phase change under all conditions. To further freeze

680 supercooled soil liquid water, however, the soil temperature has to be colder than a virtual soil temperature (as we described below). Second, due to the steep slope of  $\frac{\partial \theta_{liq}}{\partial T}$  (especially close to  $T_f = 0^\circ\text{C}$ ), the estimated ice mass increase (i.e.,  $w_{ice}^{n+1} - w_{ice}^n$  or  $w_{liq}^n - w_{liq,max}^{n+1}$ ; see (Eq. A5)) most often exceeds the required mass change, i.e.,  $H_m = -c_i \frac{\Delta z_i}{L_f} (T_f - T_i^{n+1})$ , and thus soil liquid water freezes quickly in a large chunk. Soon, the liquid water available to be frozen becomes too small to release sufficient latent heat to compensate for the required energy deficit ( $T_f - T_i^{n+1}$ ).

685

Thus, we revised the phase-change scheme mainly through incorporating a phase-change efficiency ( $\varepsilon$ ) and replacing the constant freezing point  $T_f$  with the temperature of the freezing point depression in (Eq. A2). The phase-change efficiency, introduced by Le Moigne et al. (2012) and adopted by Masson et al. (2013) and Yang et al. (2018a), is calculated as,

$$\varepsilon = \begin{cases} \varepsilon_{liq,i}^n = \frac{\theta_{liq,i}^n}{\theta_{sat,i}} & \text{for freezing} \\ \varepsilon_{ice,i}^n = \frac{\theta_{ice,i}^n}{\theta_{sat,i}} & \text{for melting} \end{cases}, \quad (\text{Eq. A9})$$

where  $\theta_{liq,i}^n$  and  $\theta_{ice,i}^n$  is the soil liquid and ice volumetric water content of layer  $i$  at previous time step  $n$ , respectively, and

690  $\theta_{sat,i}$  represents the soil porosity (i.e., the saturated volumetric water content). The temperature of the freezing point

depression, as a virtual temperature ( $Tv$ ) reversely derived from the freezing point temperature-depression equation, i.e.,

$\psi(T) = \frac{10^3 L_f (T_f - T_i)}{g T_i}$  (Fuchs et al., 1978; Cary and Mayland, 1972), is calculated as,

$$Tv_i^{n+1*} = \frac{10^3 L_f T_f}{10^3 L_f + g \psi_i^n}, \quad (\text{Eq. A10})$$

where  $L_f$  is the latent heat of fusion ( $\text{J kg}^{-1}$ ) and  $g$  is the gravitational acceleration ( $\text{m s}^{-2}$ ).  $\psi_i^n$  is the soil water potential (mm),

695 calculated as the soil water retention curve of Clapp and Hornberger (1978), i.e.,  $\psi_i^n = \psi_{sat,i} \left( \frac{\theta_{liq,i}^n}{\theta_{sat,i}} \right)^{-B_i}$ , where  $\theta_{liq,i}^n = w_{liq,i}^n / \Delta z_i$  as in (Eq. A3),  $B_i$  is the Clapp and Hornberger exponent, and  $\psi_{sat,i}$  is the soil texture-dependent saturated matric potential (mm).

Then, through multiplying the initially estimated mass change ( $H_m$ ) by the phase change efficiency ( $\varepsilon$ ), we replace the freezing  
700 point with an efficiency-weighted average of the initially solved soil temperature ( $T_i^{n+1}$ ) and the freezing point,

$$\begin{aligned} T_i^{n+1*} &= T_f \\ &+ \frac{\Delta t}{c_i \Delta z_i} \left( -c_i \frac{\Delta z_i}{\Delta t} T_{inc} \varepsilon_i + \frac{L_f (w_{ice,i}^{n+1} - w_{ice,i}^n)}{\Delta t} \right) \\ &= T_f - (T_f - T_i^{n+1}) \varepsilon_i + \frac{L_f (w_{ice,i}^{n+1} - w_{ice,i}^n)}{c_i \Delta z_i} \\ &= (1 - \varepsilon_i) T_f + \varepsilon_i T_i^{n+1} + \frac{L_f (w_{ice,i}^{n+1} - w_{ice,i}^n)}{c_i \Delta z_i} \end{aligned} \quad (\text{Eq. A11})$$

The two changes can effectively improve the soil water freezing process simulations and prevent soil becoming irreversibly too cold quickly as simulated by the baseline phase change scheme.

## Appendix B Decomposition Cascade Model

705 ELMv1-ECA explicitly simulates carbon cycle dynamics (both plant and soil) and accounts for the limitation of nutrient (i.e., nitrogen and phosphorus) availability for plant growth and the nutrient competition between plants and microbes (Burrows et al., 2020; Zhu et al., 2019; Golaz et al., 2019; Zhu et al., 2020). The ELMv1-ECA uses a Century-like soil carbon decomposition cascade model with vertically resolved soil biogeochemistry (Koven et al., 2013b), and explicitly accounts for the influence of substrate and nutrient availability on soil respiration (both root and microbes) (Zhu et al., 2019).

710

715 Within the ELMv1-ECA Century decomposition cascade model, the respiration fractions are parameterized as the fraction of the decomposition carbon flux out of each carbon pool, including litter and soil organic matter. The base decomposition rate is modified by a function representing environmental controls on soil decomposition which accounts for the impacts of individual factors including temperature ( $f_T$ ) and moisture ( $f_W$ ), an oxygen scalar ( $f_O$ ), and a depth scalar ( $f_D$ ), in a multiplicative way, i.e.,  $f_{total} = f_T f_W f_O f_D$ .

We use a  $Q_{10}$ -based standard exponential function to account for the temperature effect on decomposition,

$$f_T = Q_{10}^{\left(\frac{T-T_{ref}}{10}\right)}, \quad (\text{Eq. B12})$$

720 where  $Q_{10} = 1.5$  on default, which is consistent with ecosystem-level observations (Mahecha et al., 2010), and  $T_{ref}$  is the reference temperature (25°C). During cold seasons when soil temperature becomes subfreezing, respiration continues but with more controls from liquid water stress. The original moisture scalar ( $f_W$ ) within ELMV1-ECA is given in the formulation, calculated as,

$$f_W = \begin{cases} 0 & \text{For } \psi_i < \psi_{min} \\ \frac{\log(\psi_{min}/\psi_i)}{\log(\psi_{min}/\psi_{max})} & \text{For } \psi_{min} \leq \psi_i \leq \psi_{max} \\ 1 & \text{For } \psi_i > \psi_{max} \end{cases}, \quad (\text{Eq. B13})$$

725 where  $\psi_i = \psi_{max} \left(\frac{\theta_{liq,i}}{\theta_{sat,i}}\right)^{-B_i}$  is the soil water potential, where  $B_i$  is the Clapp and Hornberger exponent (Clapp and Hornberger, 1978). In frozen soil, the soil water potential is related to soil temperature through the freezing point depression equation, i.e.,  $\psi_i = \frac{L_f(T_f - T_i)}{10^3 T}$  (Fuchs et al., 1978; Cary and Mayland, 1972) in the supercooled water formulation (Niu and Yang, 2006). Thus, the liquid water stress on decomposition is translated into dependency on temperature when soil temperature is below the freezing point. On default,  $\psi_{min}$  is -10MPa, which predicts zero  $f_W$  under frozen conditions since  $\psi_i$  under a subfreezing soil temperature easily gets smaller than -10MPa (Figure S1a). We thus reduced the  $\psi_{min}$  to  $-10^3$  MPa and  $-10^6$  MPa to alleviate the zero respiration problem in the frozen soils (see Figure S1a). ELMv1-ECA approximates oxygen stress ( $f_O$ ) as the ratio of available oxygen to that demanded by decomposers, and has a minimum value of 0.2 (Oleson et al., 730 2013).

The depth scalar ( $f_D = \exp\left(-\frac{z_i}{Z_\tau}\right)$ ) represents unresolved other depth-dependent processes (e.g., soil microbial dynamics, priming effects, etc.) (Koven et al., 2013b; Lawrence et al., 2015; Koven et al., 2015). Applying the depth scalar to decomposition rates would exponentially decrease the respiration fluxes along with the vertical soil layers. The  $Z_\tau$  is the e- 735 folding depth for decomposition, and by default  $Z_\tau$  is 0.5 m (Oleson et al., 2013).

## Appendix C Methane Model

The ELMv1-ECA methane model includes the representations of CH<sub>4</sub> production, oxidation, and three pathways of transport (i.e., aerenchyma tissues, ebullition, aqueous and gaseous diffusion), and solves the transient reaction diffusion equation for CH<sub>4</sub>. ELMv1-ECA estimates CH<sub>4</sub> production ( $P$ ; mol m<sup>-3</sup> s<sup>-1</sup>) in the anaerobic portion of the soil column based on the upland heterotrophic respiration (HR; mol C m<sup>-2</sup> s<sup>-1</sup>) from soil and litter, further adjusted by factors representing influence from soil temperature ( $f_T$ ), pH ( $f_{pH}$ ), redox potential ( $f_{pE}$ ), and seasonal inundation condition ( $S$ ) (Riley et al., 2011), expressed as,

$$P = HR \times f_{CH_4} \times f_T \times f_{pH} \times f_{pE} \times S. \quad (\text{Eq. C14})$$

The  $f_{CH_4}$  is a fraction of anaerobically mineralized carbon atoms becoming CH<sub>4</sub> and is 0.2 on default. Detailed explanation on these factors can be found in Riley et al. (2011). The methane production  $P$  is directly related to the estimated HR and impacted by soil temperature, and thus the changes in the carbon decomposition model (Appendix B) and water and heat transfer model (Appendix A) directly influence methane production simulations. Besides, ELMv1-ECA considers the availability of carbon substrate as an important driver of methanogenesis activity and methane production (Riley et al., 2011; Xu et al., 2016).

The ultimately estimated CH<sub>4</sub> emissions are controlled by oxidation, transport mechanisms (i.e., aerenchyma transport, ebullition, and diffusion), and the upper boundary resistance. Detailed descriptions on CH<sub>4</sub> oxidation and transport mechanisms are provided in (Riley et al., 2011). Here we modified CH<sub>4</sub> transport mechanisms for facilitating reasonable cold-season CH<sub>4</sub> emissions.

Vascular plant aerenchyma tissues serve as diffusive pathways to transport CH<sub>4</sub> from soil to the atmosphere. The CH<sub>4</sub> transport via aerenchyma from soil layer  $z$  ( $A(z)$ , mol m<sup>-2</sup> s<sup>-1</sup>) is calculated as:

$$A(z) = (C(z) - C_a) / \left( \frac{r_L z}{DpT_{aere}\rho_r(z)} + r_a \right), \quad (\text{Eq. C15})$$

where  $C(z)$  and  $C_a$  is the gaseous CH<sub>4</sub> concentration (mol m<sup>-3</sup>) in soil depth  $z$  and in the atmosphere, respectively;  $r_a$  is the aerodynamic resistance (s m<sup>-1</sup>);  $D$  is the gas diffusion coefficient (m<sup>2</sup> s<sup>-1</sup>);  $p$  is aerenchyma porosity (-);  $r_L$  is the ratio of root length to vertical depth (i.e., root obliquity); and  $\rho_r(z)$  is the root fraction in soil depth  $z$  (-).  $T_{aere}$  is the specific aerenchyma area (m<sup>2</sup> m<sup>-2</sup>), and is expressed as,

$$T_{aere} = \frac{f_N N_a LAI}{0.22} \pi R^2, \quad (\text{Eq. C16})$$

where  $R$  represents the aerenchyma radius ( $=2.9 \times 10^{-3}$  m);  $N_a$  is the annual net primary production (NPP), and  $f_N$  is the belowground fraction of current NPP; and the factor 0.22 represents average observed tiller biomass (gC per tiller) (Wania et al., 2010; Schimel, 1995). In ELMv1-ECA, methane emissions through aerenchyma were turned off when the soil temperature is below 0°C. We first removed this temperature limitation; then, we integrated the emissions from ice cracks and remnants of

aerenchyma tissues with (Eq. C16) by applying a small  $\varepsilon_{aere}$  during winter time. That is,  $T_{aere} = \frac{f_{Na}\varepsilon_{aere}}{0.22} \pi R^2$  when soil  
 765 temperature is below the freezing point, where  $\varepsilon_{aere}$  represents possible ice crack fractions and remnants of aerenchyma  
 tissues, and is 0.01 on default. We also tested a larger value for this parameter together with  $f_{CH_4}$  and the maximum  $CH_4$   
 oxidation rate constant  $R_{o,max}$  (Table S3).

The  $R_{o,max}$  is a key variable controlling  $CH_4$  oxidation rate ( $R_{oxic}$ ), calculated as,

$$R_{oxic} = R_{o,max} \left[ \frac{C_{CH_4}}{K_{CH_4} + C_{CH_4}} \right] \left[ \frac{C_{O_2}}{K_{O_2} + C_{O_2}} \right] Q_{10} F_v, \quad (\text{Eq. C17})$$

770 where  $C_{CH_4}$  and  $C_{O_2}$  are  $CH_4$  and  $O_2$  concentrations, respectively;  $K_{CH_4}$  and  $K_{O_2}$  are the half saturation coefficients ( $\text{mol m}^{-3}$ )  
 for  $C_{CH_4}$  and  $C_{O_2}$ , respectively. Details about the  $CH_4$  oxidation is provided in Riley et al. (2011). The maximum oxidation  
 rate  $R_{o,max}$  ( $\text{mol m}^{-3} \text{s}^{-1}$ ) by default is 1.25E-05 and 1.25E-06 for saturated and unsaturated conditions, respectively. We tested  
 the  $R_{o,max}$  with the smaller value (1.25E-06) for saturated condition as well (Table S3).

Another key variable that is highly uncertain is snow resistance to gas emissions. When snow is present, the upper boundary  
 layer resistance to gas emissions is added by a snow resistance accounting for diffusion through the snow based on the  
 Millington-Quirk expression (Riley et al. (2011)). However, we found the computed snow resistance generally was too large.  
 We thus decreased snow resistance by introducing new scale factor, i.e.,  $\varepsilon_{snowdiff}$  ( $10^2$  on default) to increase the conductance  
 780 at the upper boundary when snow is present.

## References

- Anthony, K. M. W., Anthony, P., Grosse, G., and Chanton, J.: Geologic methane seeps along boundaries of Arctic  
 permafrost thaw and melting glaciers, *Nat Geosci*, 5, 419-426, 2012.
- 785 Arndt, K. A., Oechel, W. C., Goodrich, J. P., Bailey, B. A., Kalhori, A., Hashemi, J., Sweeney, C., and Zona, D.:  
 Sensitivity of Methane Emissions to Later Soil Freezing in Arctic Tundra Ecosystems, *J Geophys Res-  
 Biogeo*, 124, 2595-2609, 10.1029/2019JG005242, 2019.
- Belshe, E. F., Schuur, E. A. G., and Bolker, B. M.: Tundra ecosystems observed to be  $CO_2$  sources due to  
 differential amplification of the carbon cycle, *Ecol Lett*, 16, 1307-1315, 10.1111/ele.12164, 2013.
- 790 Bhanja, S. N., and Wang, J. Y.: Estimating influences of environmental drivers on soil heterotrophic respiration in  
 the Athabasca River Basin, Canada, *Environ Pollut*, 257, 2020.
- Bisht, G., Riley, W. J., Wainwright, H. M., Dafflon, B., Yuan, F. M., and Romanovsky, V. E.: Impacts of  
 microtopographic snow redistribution and lateral subsurface processes on hydrologic and thermal states in  
 an Arctic polygonal ground ecosystem: a case study using ELM-3D v1.0, *Geosci Model Dev*, 11, 61-76,  
 795 2018.
- Box, J. E., Colgan, W. T., Christensen, T. R., Schmidt, N. M., Lund, M., Parmentier, F. J. W., Brown, R., Bhatt,  
 U. S., Euskirchen, E. S., Romanovsky, V. E., Walsh, J. E., Overland, J. E., Wang, M. Y., Corell, R. W.,

- Meier, W. N., Wouters, B., Mernild, S., Mard, J., Pawlak, J., and Olsen, M. S.: Key indicators of Arctic climate change: 1971-2017, *Environmental Research Letters*, 14, 2019.
- 800 Burrows, S. M., Maltrud, M., Yang, X., Zhu, Q., Jeffery, N., Shi, X., Ricciuto, D., Wang, S., Bisht, G., Tang, J., Wolfe, J., Harrop, B. E., Singh, B., Brent, L., Baldwin, S., Zhou, T., Cameron-Smith, P., Keen, N., Collier, N., Xu, M., Hunke, E. C., Elliott, S. M., Turner, A. K., Li, H., Wang, H., Golaz, J. C., Bond-Lamberty, B., Hoffman, F. M., Riley, W. J., Thornton, P. E., Calvin, K., and Leung, L. R.: The DOE E3SM v1.1 Biogeochemistry Configuration: Description and Simulated Ecosystem-Climate Responses to Historical Changes in Forcing, *J Adv Model Earth Sy*, 12, 2020.
- 805 Cary, J. W., and Mayland, H. F.: Salt and Water Movement in Unsaturated Frozen Soil, *Soil Sci Soc Am Pro*, 36, 549-&, 1972.
- Chang, K. Y., Riley, W. J., Crill, P. M., Grant, R. F., Rich, V. I., and Saleska, S. R.: Large carbon cycle sensitivities to climate across a permafrost thaw gradient in subarctic Sweden, *Cryosphere*, 13, 647-663, 2019.
- 810 Chang, K. Y., Riley, W. J., Crill, P. M., Grant, R. F., and Saleska, S. R.: Hysteretic temperature sensitivity of wetland CH<sub>4</sub> fluxes explained by substrate availability and microbial activity, *Biogeosciences*, 17, 5849-5860, 2020.
- Chang, K. Y., Riley, W. J., Knox, S. H., Jackson, R. B., and al., e.: Substantial hysteresis in emergent temperature sensitivity of global wetland CH<sub>4</sub> emissions, (Under Review), 2021.
- 815 Clapp, R. B., and Hornberger, G. M.: Empirical equations for some soil hydraulic properties, *Water Resources Research*, 14, 601-604, 1978.
- Commane, R., Lindaas, J., Benmergui, J., Luus, K. A., Chang, R. Y. W., Daube, B. C., Euskirchen, E. S., Henderson, J. M., Karion, A., Miller, J. B., Miller, S. M., Parazoo, N. C., Randerson, J. T., Sweeney, C., Tans, P., Thoning, K., Veraverbeke, S., Miller, C. E., and Wofsy, S. C.: Carbon dioxide sources from Alaska driven by increasing early winter respiration from Arctic tundra, *P Natl Acad Sci USA*, 114, 5361-5366, 2017.
- 820 Dankers, R., Burke, E. J., and Price, J.: Simulation of permafrost and seasonal thaw depth in the JULES land surface scheme, *Cryosphere*, 5, 773-790, 2011.
- Davidson, E. A., and Janssens, I. A.: Temperature sensitivity of soil carbon decomposition and feedbacks to climate change, *Nature*, 440, 165-173, 2006.
- 825 Davidson, S. J., and Zona, D.: Arctic Vegetation Plots in Flux Tower Footprints, North Slope, Alaska, 2014, ORNL DAAC, Oak Ridge, Tennessee, USA. <https://doi.org/10.3334/ORNLDAAC/1546>, 2018.
- Delwiche, K. B., Knox, S. H., Malhotra, A., Fluet-Chouinard, E., McNicol, G., Feron, S., Ouyang, Z., Papale, D., Trotta, C., and Canfora, E.: FLUXNET-CH<sub>4</sub>: A global, multi-ecosystem dataset and analysis of methane seasonality from freshwater wetlands, *Earth System Science Data Discussions*, 1-111, 2021.
- 830 Etiope, G., and Klusman, R. W.: Microseepage in drylands: Flux and implications in the global atmospheric source/sink budget of methane, *Global and Planetary Change*, 72, 265-274, 2010.
- Fahnestock, J. T., Jones, M. H., Brooks, P. D., Walker, D. A., and Welker, J. M.: Winter and early spring CO<sub>2</sub> efflux from tundra communities of northern Alaska, *Journal of Geophysical Research-Atmospheres*, 103, 29023-29027, Doi 10.1029/98jd00805, 1998.
- 835 Fuchs, M., Campbell, G., and Papendick, R.: An analysis of sensible and latent heat flow in a partially frozen unsaturated soil, *Soil Sci Soc Am J*, 42, 379-385, 1978.
- Golaz, J. C., Caldwell, P. M., Van Roekel, L. P., Petersen, M. R., Tang, Q., Wolfe, J. D., Abeshu, G., Anantharaj, V., Asay-Davis, X. S., Bader, D. C., Baldwin, S. A., Bisht, G., Bogenschütz, P. A., Branstetter, M., Brunke, M. A., Brus, S. R., Burrows, S. M., Cameron-Smith, P. J., Donahue, A. S., Deakin, M., Easter, R. C., Evans, K. J., Feng, Y., Flanner, M., Foucar, J. G., Fyke, J. G., Griffin, B. M., Hannay, C., Harrop, B. E., Hoffman, M. J., Hunke, E. C., Jacob, R. L., Jacobsen, D. W., Jeffery, N., Jones, P. W., Keen, N. D., Klein, S. A., Larson, V. E., Leung, L. R., Li, H. Y., Lin, W. Y., Lipscomb, W. H., Ma, P. L., Mahajan, S., Maltrud,
- 840

- 845 M. E., Mametjanov, A., McClean, J. L., McCoy, R. B., Neale, R. B., Price, S. F., Qian, Y., Rasch, P. J.,  
Eyre, J. E. J. R., Riley, W. J., Ringer, T. D., Roberts, A. F., Roesler, E. L., Salinger, A. G., Shaheen, Z.,  
Shi, X. Y., Singh, B., Tang, J. Y., Taylor, M. A., Thornton, P. E., Turner, A. K., Veneziani, M., Wan, H.,  
Wang, H. L., Wang, S. L., Williams, D. N., Wolfram, P. J., Worley, P. H., Xie, S. C., Yang, Y., Yoon, J.  
H., Zelinka, M. D., Zender, C. S., Zeng, X. B., Zhang, C. Z., Zhang, K., Zhang, Y., Zheng, X., Zhou, T.,  
and Zhu, Q.: The DOE E3SM Coupled Model Version 1: Overview and Evaluation at Standard Resolution,  
850 *J Adv Model Earth Sy*, 11, 2089-2129, 2019.
- Graf, A., Weihermuller, L., Huisman, J. A., Herbst, M., and Vereecken, H.: Comment on "Global Convergence in  
the Temperature Sensitivity of Respiration at Ecosystem Level", *Science*, 331, 1265-+, 2011.
- Grant, R. F., Mekonnen, Z. A., Riley, W. J., Arora, B., and Torn, M. S.: Mathematical Modelling of Arctic  
855 Polygonal Tundra with Ecosys: 2. Microtopography Determines How CO<sub>2</sub> and CH<sub>4</sub> Exchange Responds  
to Changes in Temperature and Precipitation, *J Geophys Res-Bioge*, 122, 3174-3187, 2017a.
- Grant, R. F., Mekonnen, Z. A., Riley, W. J., Wainwright, H. M., Graham, D., and Torn, M. S.: Mathematical  
Modelling of Arctic Polygonal Tundra with Ecosys: 1. Microtopography Determines How Active Layer  
860 Depths Respond to Changes in Temperature and Precipitation, *J Geophys Res-Bioge*, 122, 3161-3173,  
2017b.
- Harmon, M., and Domingo, J.: A users guide to STANDCARB version 2.0: a model to simulate the carbon stores  
in forest stands, Dep. of For. Sci., Oreg. State Univ., Corvallis, OR, 2001.
- Harris, I.: CRU JRA v1. 1: A forcings dataset of gridded land surface blend of Climatic Research Unit (CRU) and  
Japanese reanalysis (JRA) data; Jan. 1901-Dec. 2017. Published by: University of East Anglia Climatic  
865 Research Unit, Centre for Environmental Data Analysis, 2905 doi:  
10.5285/13f3635174794bb98cf8ac4b0ee8f4ed, 2019.
- Jones, M. H., Fahnestock, J. T., and Welker, J. M.: Early and late winter CO<sub>2</sub> efflux from arctic tundra in the  
Kuparuk River watershed, Alaska, USA, *Arct Antarct Alp Res*, 31, 187-190, Doi 10.2307/1552607, 1999.
- Kelly, R., Parton, W., Hartman, M., Stretch, L., Ojima, D., and Schimel, D.: Intra-annual and interannual variability  
of ecosystem processes in shortgrass steppe, *Journal of Geophysical Research: Atmospheres*, 105, 20093-  
870 20100, 2000.
- Kim, D., Lee, M. I., and Seo, E.: Improvement of Soil Respiration Parameterization in a Dynamic Global  
Vegetation Model and Its Impact on the Simulation of Terrestrial Carbon Fluxes, *Journal of Climate*, 32,  
127-143, 2019.
- Kim, Y., Ueyama, M., Nakagawa, F., Tsunogai, U., Harazono, Y., and Tanaka, N.: Assessment of winter fluxes of  
875 CO<sub>2</sub> and CH<sub>4</sub> in boreal forest soils of central Alaska estimated by the profile method and the chamber  
method: a diagnosis of methane emission and implications for the regional carbon budget, *Tellus B:  
Chemical and Physical Meteorology*, 59, 223-233, 2007.
- Kittler, F., Heimann, M., Kolle, O., Zimov, N., Zimov, S., and Gockede, M.: Long-Term Drainage Reduces CO<sub>2</sub>  
Uptake and CH<sub>4</sub> Emissions in a Siberian Permafrost Ecosystem, *Global Biogeochemical Cycles*, 31, 1704-  
880 1717, 2017.
- Knox, S. H., Jackson, R. B., Poulter, B., McNicol, G., Fluet-Chouinard, E., Zhang, Z., Hugelius, G., Bousquet, P.,  
Canadell, J. G., Saunio, M., Papale, D., Chu, H., Keenan, T. F., Baldocchi, D., Torn, M. S., Mammarella,  
I., Trotta, C., Aurela, M., Bohrer, G., Campbell, D. I., Cescatti, A., Chamberlain, S., Chen, J., Chen, W.,  
Dengel, S., Desai, A. R., Euskirchen, E., Friborg, T., Gasbarra, D., Godeed, I., Goeckede, M., Heimann, M.,  
885 Helbig, M., Hirano, T., Hollinger, D. Y., Iwata, H., Kang, M., Klatt, J., Krauss, K. W., Kutzbach, L., Lohila,  
A., Mitra, B., Morin, T. H., Nilsson, M. B., Niu, S., Noormets, A., Oechel, W. C., Peichl, M., Peltola, O.,  
Reba, M. L., Richardson, A. D., Runkle, B. R. K., Ryu, Y., Sachs, T., Schafer, K. V. R., Schmid, H. P.,  
Shurpali, N., Sonntag, O., Tang, A. C. I., Ueyama, M., Vargas, R., Vesala, T., Ward, E. J., Windham-  
Myers, L., Wohlfahrt, G., and Zona, D.: FLUXNET-CH<sub>4</sub> Synthesis Activity: Objectives, Observations,

- 890 and Future Directions, *Bulletin of the American Meteorological Society*, 100, 2607-2632, 10.1175/Bams-D-18-0268.1, 2019.
- Koven, C. D., Ringeval, B., Friedlingstein, P., Ciais, P., Cadule, P., Khvorostyanov, D., Krinner, G., and Tarnocai, C.: Permafrost carbon-climate feedbacks accelerate global warming, *P Natl Acad Sci USA*, 108, 14769-14774, 2011.
- 895 Koven, C. D., Riley, W. J., and Stern, A.: Analysis of Permafrost Thermal Dynamics and Response to Climate Change in the CMIP5 Earth System Models, *Journal of Climate*, 26, 1877-1900, 10.1175/Jcli-D-12-00228.1, 2013a.
- Koven, C. D., Riley, W. J., Subin, Z. M., Tang, J. Y., Torn, M. S., Collins, W. D., Bonan, G. B., Lawrence, D. M., and Swenson, S. C.: The effect of vertically resolved soil biogeochemistry and alternate soil C and N  
900 models on C dynamics of CLM4, *Biogeosciences*, 10, 7109-7131, 2013b.
- Koven, C. D., Lawrence, D. M., and Riley, W. J.: Permafrost carbon-climate feedback is sensitive to deep soil carbon decomposability but not deep soil nitrogen dynamics, *P Natl Acad Sci USA*, 112, 3752-3757, 10.1073/pnas.1415123112, 2015.
- Koven, C. D., Hugelius, G., Lawrence, D. M., and Wieder, W. R.: Higher climatological temperature sensitivity of  
905 soil carbon in cold than warm climates, *Nat Clim Change*, 7, 817-+, 10.1038/Nclimate3421, 2017.
- Kuhn, M. A., Varner, R. K., Bastviken, D., Crill, P., MacIntyre, S., Turetsky, M., Walter Anthony, K., McGuire, A. D., and Olefeldt, D.: BAWLD-CH 4: A Comprehensive Dataset of Methane Fluxes from Boreal and Arctic Ecosystems, *Earth System Science Data Discussions*, 1-56, 2021.
- Kurylyk, B. L., and Hayashi, M.: Improved Stefan Equation Correction Factors to Accommodate Sensible Heat  
910 Storage during Soil Freezing or Thawing, *Permafrost Periglac*, 27, 189-203, 2016.
- Lawrence, D. M., Thornton, P. E., Oleson, K. W., and Bonan, G. B.: The partitioning of evapotranspiration into transpiration, soil evaporation, and canopy evaporation in a GCM: Impacts on land-atmosphere interaction, *J. Hydrometeorol.*, 8, 862-880, 2007.
- Lawrence, D. M., and Slater, A. G.: Incorporating organic soil into a global climate model, *Clim Dynam*, 30, 145-  
915 160, 10.1007/s00382-007-0278-1, 2008.
- Lawrence, D. M., Koven, C. D., Swenson, S. C., Riley, W. J., and Slater, A. G.: Permafrost thaw and resulting soil moisture changes regulate projected high-latitude CO<sub>2</sub> and CH<sub>4</sub> emissions, *Environmental Research Letters*, 10, 10.1088/1748-9326/10/9/094011, 2015.
- Le Moigne, P., Boone, A., Belamari, S., Brun, E., Calvet, J., Decharme, B., Faroux, S., Gibelin, A., Giordani, H.,  
920 Lafont, S., Lebeaupin, C., Le Moigne, P., Mahfouf, J., Martin, E., Masson, V., Mironov, D., Morin, S., Noilhan, J., Tulet, P., Van den Hurk, B., and Vionnet, V.: SURFEX Scientific Documentation, Note de centre (CNRM/GMME), Météo-France, Toulouse, France, 2012.
- Liu, Y. N., Bisht, G., Subin, Z. M., Riley, W. J., and Pau, G. S. H.: A Hybrid Reduced-Order Model of Fine-Resolution Hydrologic Simulations at a Polygonal Tundra Site, *Vadose Zone J*, 15, 2016.
- 925 Lyman, S. N., Tran, H. N., Mansfield, M. L., Bowers, R., and Smith, A.: Strong temporal variability in methane fluxes from natural gas well pad soils, *Atmospheric Pollution Research*, 2020.
- Mahecha, M. D., Reichstein, M., Carvalhais, N., Lasslop, G., Lange, H., Seneviratne, S. I., Vargas, R., Ammann, C., Arain, M. A., Cescatti, A., Janssens, I. A., Migliavacca, M., Montagnani, L., and Richardson, A. D.: Global Convergence in the Temperature Sensitivity of Respiration at Ecosystem Level, *Science*, 329, 838-  
930 840, 2010.
- Masson, V., Le Moigne, P., Martin, E., Faroux, S., Alias, A., Alkama, R., Belamari, S., Barbu, A., Boone, A., Bouyssel, F., Brousseau, P., Brun, E., Calvet, J. C., Carrer, D., Decharme, B., Delire, C., Donier, S., Essaouini, K., Gibelin, A. L., Giordani, H., Habets, F., Jidane, M., Kerdraon, G., Kourzeneva, E., Lafaysse, M., Lafont, S., Brossier, C. L., Lemonsu, A., Mahfouf, J. F., Marguinaud, P., Mokhtari, M., Morin, S.,  
935 Pigeon, G., Salgado, R., Seity, Y., Taillefer, F., Tanguy, G., Tulet, P., Vincendon, B., Vionnet, V., and

- Voldoire, A.: The SURFEXv7.2 land and ocean surface platform for coupled or offline simulation of earth surface variables and fluxes, *Geosci Model Dev*, 6, 929-960, 2013.
- Mastepanov, M., Sigsgaard, C., Dlugokencky, E. J., Houweling, S., Strom, L., Tamstorf, M. P., and Christensen, T. R.: Large tundra methane burst during onset of freezing, *Nature*, 456, 628-U658, 2008.
- 940 Mekonnen, Z. A., Riley, W. J., Grant, R. F., and Romanovsky, V.: Changes in precipitation and air temperature contribute comparably to permafrost degradation in a warmer climate, *Environ Res Lett*, 2020.
- Meyer, N., Welp, G., and Amelung, W.: The Temperature Sensitivity (Q10) of Soil Respiration: Controlling Factors and Spatial Prediction at Regional Scale Based on Environmental Soil Classes, *Global Biogeochemical Cycles*, 32, 306-323, 2018.
- 945 Moriasi, D. N., Arnold, J. G., Van Liew, M. W., Bingner, R. L., Harmel, R. D., and Veith, T. L.: Model evaluation guidelines for systematic quantification of accuracy in watershed simulations, *Transactions of the Asabe*, 50, 885-900, 2007.
- Moyano, F. E., Manzoni, S., and Chenu, C.: Responses of soil heterotrophic respiration to moisture availability: An exploration of processes and models, *Soil Biol Biochem*, 59, 72-85, 2013.
- 950 Nash, J. E., and Sutcliffe, J. V.: River flow forecasting through conceptual models part I — A discussion of principles, *J. Hydrol.*, 10, 282-290, 10.1016/0022-1694(70)90255-6, 1970.
- Natali, S. M., Watts, J. D., Rogers, B. M., Potter, S., Ludwig, S. M., Selbmann, A.-K., Sullivan, P. F., Abbott, B. W., Arndt, K. A., Birch, L., Björkman, M. P., Bloom, A. A., Celis, G., Christensen, T. R., Christiansen, C. T., Commene, R., Cooper, E. J., Crill, P., Czimeczik, C., Davydov, S., Du, J., Egan, J. E., Elberling, B.,
- 955 Euskirchen, E. S., Friborg, T., Genet, H., Göckede, M., Goodrich, J. P., Grogan, P., Helbig, M., Jafarov, E. E., Jastrow, J. D., Kalhori, A. A. M., Kim, Y., Kimball, J. S., Kutzbach, L., Lara, M. J., Larsen, K. S., Lee, B.-Y., Liu, Z., Loranty, M. M., Lund, M., Lupascu, M., Madani, N., Malhotra, A., Matamala, R., McFarland, J., McGuire, A. D., Michelsen, A., Minions, C., Oechel, W. C., Olefeldt, D., Parmentier, F.-J. W., Pirk, N., Poulter, B., Quinton, W., Rezanezhad, F., Risk, D., Sachs, T., Schaefer, K., Schmidt, N. M.,
- 960 Schuur, E. A. G., Semenchuk, P. R., Shaver, G., Sonnentag, O., Starr, G., Treat, C. C., Waldrop, M. P., Wang, Y., Welker, J., Wille, C., Xu, X., Zhang, Z., Zhuang, Q., and Zona, D.: Large loss of CO<sub>2</sub> in winter observed across the northern permafrost region, *Nat Clim Change*, 10.1038/s41558-019-0592-8, 2019.
- Neumann, R. B., Moorberg, C. J., Lundquist, J. D., Turner, J. C., Waldrop, M. P., McFarland, J. W., Euskirchen, E. S., Edgar, C. W., and Turetsky, M. R.: Warming effects of spring rainfall increase methane emissions from thawing permafrost, *Geophys Res Lett*, 2019.
- 965 Nicolsky, D. J., Romanovsky, V. E., Alexeev, V. A., and Lawrence, D. M.: Improved modeling of permafrost dynamics in a GCM land-surface scheme, *Geophys Res Lett*, 34, 2007.
- Niu, G. Y., and Yang, Z. L.: Effects of frozen soil on snowmelt runoff and soil water storage at a continental scale, *J. Hydrometeorol.*, 7, 937-952, 2006.
- 970 Oechel, W. C., Vourlitis, G. L., Hastings, S. J., Zulueta, R. C., Hinzman, L., and Kane, D.: Acclimation of ecosystem CO<sub>2</sub> exchange in the Alaskan Arctic in response to decadal climate warming, *Nature*, 406, 978-981, 2000.
- Oechel, W. C., Laskowski, C. A., Burba, G., Gioli, B., and Kalhori, A. A. M.: Annual patterns and budget of CO<sub>2</sub> flux in an Arctic tussock tundra ecosystem, *J Geophys Res-Bioge*, 119, 323-339, 2014.
- 975 Oechel, W. C., and Kalhori, A.: ABoVE: CO<sub>2</sub> and CH<sub>4</sub> Fluxes and Meteorology at Flux Tower Sites, Alaska, 2015-2017, <https://doi.org/10.3334/ornladaac/1562>, 2018.
- Oleson, K. W., Lawrence, D., Bonan, G., Drewniak, B., Huang, M., Koven, C., Levis, S., Li, F., Riley, W., and Subin, Z.: Technical Description of version 4.5 of the Community Land Model (CLM)(NCAR Technical Note No. NCAR/TN-503+ STR). Citeseer, National Center for Atmospheric Research, PO Box, 3000,
- 980 2013.

- Outcalt, S. I., Nelson, F. E., and Hinkel, K. M.: The Zero-Curtain Effect - Heat and Mass-Transfer across an Isothermal Region in Freezing Soil, *Water Resources Research*, 26, 1509-1516, 1990.
- Pau, G. S. H., Shen, C. P., Riley, W. J., and Liu, Y. N.: Accurate and efficient prediction of fine-resolution hydrologic and carbon dynamic simulations from coarse-resolution models, *Water Resources Research*, 52, 791-812, 2016.
- 985 Peltola, O., Vesala, T., Gao, Y., Raty, O., Alekseychik, P., Aurela, M., Chojnicki, B., Desai, A. R., Dolman, A. J., Euskirchen, E. S., Friborg, T., Gockede, M., Helbig, M., Humphreys, E., Jackson, R. B., Jocher, G., Joos, F., Klatt, J., Knox, S. H., Kowalska, N., Kutzbach, L., Lienert, S., Lohila, A., Mammarella, I., Nadeau, D. F., Nilsson, M. B., Oechel, W. C., Peichl, M., Pypker, T., Quinton, W., Rinne, J., Sachs, T., Samson, M., Schmid, H. P., Sonnentag, O., Wille, C., Zona, D., and Aalto, T.: Monthly gridded data product of northern wetland methane emissions based on upscaling eddy covariance observations, *Earth Syst Sci Data*, 11, 1263-1289, 10.5194/essd-11-1263-2019, 2019.
- 990 Piao, S. L., Ciais, P., Friedlingstein, P., Peylin, P., Reichstein, M., Luyssaert, S., Margolis, H., Fang, J. Y., Barr, A., Chen, A. P., Grelle, A., Hollinger, D. Y., Laurila, T., Lindroth, A., Richardson, A. D., and Vesala, T.: Net carbon dioxide losses of northern ecosystems in response to autumn warming, *Nature*, 451, 49-U43, 2008.
- 995 Pirk, N., Mastepanov, M., Loez-Blanco, E., Christensen, L. H., Christiansen, H. H., Hansen, B. U., Lund, M., Parmentier, F. J. W., Skov, K., and Christensen, T. R.: Toward a statistical description of methane emissions from arctic wetlands, *Ambio*, 46, S70-S80, 2017.
- 1000 Rafique, R., Xia, J. Y., Hararuk, O., Asrar, G. R., Leng, G. Y., Wang, Y. P., and Luo, Y. Q.: Divergent predictions of carbon storage between two global land models: attribution of the causes through traceability analysis, *Earth Syst Dynam*, 7, 2016.
- Riley, W. J., Subin, Z. M., Lawrence, D. M., Swenson, S. C., Torn, M. S., Meng, L., Mahowald, N. M., and Hess, P.: Barriers to predicting changes in global terrestrial methane fluxes: analyses using CLM4Me, a methane biogeochemistry model integrated in CESM, *Biogeosciences*, 8, 1925-1953, 10.5194/bg-8-1925-2011, 2011.
- 1005 Romanovsky, V. E., Kholodov, A. L., Cable, W. L., Cohen, L., Panda, S., Marchenko, S., Muskett, R. R., and Nicolsky, D.: Network of Permafrost Observatories in North America and Russia, 10.18739/A2SH27, 2009.
- 1010 Russell, S. J., Bohrer, G., Johnson, D. R., Villa, J. A., Heltzel, R., Rey-Sanchez, C., and Matthes, J. H.: Quantifying CH<sub>4</sub> concentration spikes above baseline and attributing CH<sub>4</sub> sources to hydraulic fracturing activities by continuous monitoring at an off-site tower, *Atmos Environ*, 117452, 2020.
- Sapriza-Azuri, G., Gamazo, P., Razavi, S., and Wheeler, H. S.: On the appropriate definition of soil profile configuration and initial conditions for land surface-hydrology models in cold regions, *Hydrol Earth Syst Sc*, 22, 3295-3309, 10.5194/hess-22-3295-2018, 2018.
- 1015 Schimel, J. P.: Plant-Transport and Methane Production as Controls on Methane Flux from Arctic Wet Meadow Tundra, *Biogeochemistry*, 28, 183-200, 1995.
- Sierra, C. A., Trumbore, S. E., Davidson, E. A., Vicca, S., and Janssens, I.: Sensitivity of decomposition rates of soil organic matter with respect to simultaneous changes in temperature and moisture, *J Adv Model Earth Sy*, 7, 335-356, 2015.
- 1020 Sierra, C. A., Malghani, S., and Loescher, H. W.: Interactions among temperature, moisture, and oxygen concentrations in controlling decomposition rates in a boreal forest soil, *Biogeosciences*, 14, 703-710, 2017.
- Skopp, J., Jawson, M., and Doran, J.: Steady-state aerobic microbial activity as a function of soil water content, *Soil Sci Soc Am J*, 54, 1619-1625, 1990.
- 1025

- Tang, J. Y., and Riley, W. J.: Weaker soil carbon-climate feedbacks resulting from microbial and abiotic interactions, *Nat Clim Change*, 5, 56-60, 10.1038/Nclimate2438, 2015.
- Tang, J. Y., and Riley, W. J.: A Theory of Effective Microbial Substrate Affinity Parameters in Variably Saturated Soils and an Example Application to Aerobic Soil Heterotrophic Respiration, *J Geophys Res-Biogeophys*, 124, 918-940, 2019.
- 1030 Tao, J., Reichle, R. H., Koster, R. D., Forman, B. A., and Xue, Y.: Evaluation and Enhancement of Permafrost Modeling With the NASA Catchment Land Surface Model, *J Adv Model Earth Sy*, 9, 2771-2795, 2017.
- Tao, J., Koster, R. D., Reichle, R. H., Forman, B. A., Xue, Y., Chen, R. H., and Moghaddam, M.: Permafrost variability over the Northern Hemisphere based on the MERRA-2 reanalysis, *The Cryosphere*, 13, 2087-2110, 2019.
- 1035 Tao, J., Zhu, Q., Riley, W. J., and Neumann, R. B.: Warm-season net CO<sub>2</sub> uptake outweighs cold-season emissions over Alaskan North Slope tundra under current and RCP8.5 climate *Environmental Research Letters*, (Accepted), 2021.
- Taylor, M. A., Celis, G., Ledman, J. D., Bracho, R., and Schuur, E. A. G.: Methane Efflux Measured by Eddy Covariance in Alaskan Upland Tundra Undergoing Permafrost Degradation, *J Geophys Res-Biogeophys*, 123, 2695-2710, 2018.
- 1040 Virkkala, A.-M., Aalto, J. A., Tagesson, T., Treat, C. C., Lehtonen, A., Rogers, B. M., Natali, S., and Luoto, M.: High-latitude terrestrial regions remain a CO<sub>2</sub> sink over 1990-2015, *AGUFM*, 2019, B43E-01, 2019.
- Virkkala, A. M., Aalto, J., Rogers, B. M., Tagesson, T., Treat, C. C., Natali, S. M., Watts, J. D., Potter, S., Lehtonen, A., and Mauritz, M.: Statistical upscaling of ecosystem CO<sub>2</sub> fluxes across the terrestrial tundra and boreal domain: regional patterns and uncertainties, *Global Change Biol*, 2021.
- 1045 Wang, Y. H., Yuan, F. M., Yuan, F. H., Gu, B. H., Hahn, M. S., Torn, M. S., Ricciuto, D. M., Kumar, J., He, L. Y., Zona, D., Lipson, D. A., Wagner, R., Oechel, W. C., Wullschleger, S. D., Thornton, P. E., and Xu, X. F.: Mechanistic Modeling of Microtopographic Impacts on CO<sub>2</sub> and CH<sub>4</sub> Fluxes in an Alaskan Tundra Ecosystem Using the CLM-Microbe Model, *J Adv Model Earth Sy*, 11, 4288-4304, 2019.
- 1050 Wania, R., Ross, I., and Prentice, I. C.: Implementation and evaluation of a new methane model within a dynamic global vegetation model: LPJ-WHyMe v1.3.1, *Geosci Model Dev*, 3, 565-584, 2010.
- Wilkman, E., Zona, D., Tang, Y. F., Gioli, B., Lipson, D. A., and Oechel, W.: Temperature Response of Respiration Across the Heterogeneous Landscape of the Alaskan Arctic Tundra, *J Geophys Res-Biogeophys*, 123, 2287-2302, 2018.
- 1055 Xu, X. Y., Riley, W. J., Koven, C. D., Billesbach, D. P., Chang, R. Y. W., Commane, R., Euskirchen, E. S., Hartery, S., Harazono, Y., Iwata, H., McDonald, K. C., Miller, C. E., Oechel, W. C., Poulter, B., Raz-Yaseef, N., Sweeney, C., Torn, M., Wofsy, S. C., Zhang, Z., and Zona, D.: A multi-scale comparison of modeled and observed seasonal methane emissions in northern wetlands, *Biogeosciences*, 13, 5043-5056, 10.5194/bg-13-5043-2016, 2016.
- 1060 Yan, Z. F., Bond-Lamberty, B., Todd-Brown, K. E., Bailey, V. L., Li, S. L., Liu, C. Q., and Liu, C. X.: A moisture function of soil heterotrophic respiration that incorporates microscale processes, *Nat Commun*, 9, 2018.
- Yang, K., Wang, C. H., and Li, S. Y.: Improved Simulation of Frozen-Thawing Process in Land Surface Model (CLM4.5), *Journal of Geophysical Research-Atmospheres*, 123, 13238-13258, 2018a.
- 1065 Yang, Q., Dan, L., Wu, J., Jiang, R., Dan, J., Li, W., Yang, F., Yang, X., and Xia, L.: The Improved Freeze-Thaw Process of a Climate-Vegetation Model: Calibration and Validation Tests in the Source Region of the Yellow River, *Journal of Geophysical Research-Atmospheres*, 123, 13346-13367, 2018b.
- Zeng, J. Y., Matsunaga, T., Tan, Z. H., Saigusa, N., Shirai, T., Tang, Y. H., Peng, S. S., and Fukuda, Y.: Global terrestrial carbon fluxes of 1999-2019 estimated by upscaling eddy covariance data with a random forest, *Scientific Data*, 7, 2020.
- 1070

- Zhou, T., Shi, P. J., Hui, D. F., and Luo, Y. Q.: Global pattern of temperature sensitivity of soil heterotrophic respiration ( $Q_{10}$ ) and its implications for carbon-climate feedback, *J Geophys Res-Biogeosci*, 114, 2009.
- 1075 Zhu, Q., Riley, W. J., Tang, J. Y., Collier, N., Hoffman, F. M., Yang, X. J., and Bisht, G.: Representing Nitrogen, Phosphorus, and Carbon Interactions in the E3SM Land Model: Development and Global Benchmarking, *J Adv Model Earth Sy*, 11, 2238-2258, 2019.
- Zhu, Q., Riley, W. J., Iversen, C. M., and Kattge, J.: Assessing Impacts of Plant Stoichiometric Traits on Terrestrial Ecosystem Carbon Accumulation Using the E3SM Land Model, *J Adv Model Earth Sy*, 12, 2020.
- 1080 Zona, D., Gioli, B., Commane, R., Lindaas, J., Wofsy, S. C., Miller, C. E., Dinardo, S. J., Dengel, S., Sweeney, C., and Karion, A.: Cold season emissions dominate the Arctic tundra methane budget, *Proceedings of the National Academy of Sciences*, 113, 40-45, 2016.

**Table 1: Specific modifications made to ELMv1-ECA.**

	<b>Part 1 – Phase-change scheme within the heat transfer module</b>		<b>Part 2 – Environmental modifier to the base decomposition rate</b>		<b>Part 3 – Methane module</b>	
Relevant processes influenced	Water and heat transfer, plant and soil respiration, plant productivity, CO <sub>2</sub> fluxes and CH <sub>4</sub> emissions.		Plant and soil respiration, plant productivity, CO <sub>2</sub> fluxes and CH <sub>4</sub> emissions.		CH <sub>4</sub> emissions	
	Original	New	Original	New	Original	New
Variables or equations influenced	Eq. A2-6	Imposing Eq. A7 and Eq. A8 to Eq. A2-A6	Eq. B9-B10	Eq. B11 and changes in Table S2	Eq. C13-C17	<ol style="list-style-type: none"> <li>1. Introducing a new factor <math>\epsilon_{aere}</math>, representing possible pathways via ice crack fractions and remnants of aerenchyma tissues in frozen soils, and thus permitting transport even when temperature is below 0°C.</li> <li>2. Introducing new scale factors for snow resistance <math>\epsilon_{snowdiff}</math>.</li> <li>3. Seven parameterizations combining tested values for three highly uncertain variables, i.e., <math>f_{CH_4}</math>, <math>\epsilon_{aere}</math>, and <math>R_{o,max}</math> (Table S3).</li> </ol>

**Table 2: List of Designed Experiments.**

Experiment Name	Part 1 - Phase Change Scheme within Heat Transfer Model		Part 2 – Environmental Modifier within Carbon Decomposition Model		Part 3 – Methane Model	
	Original	New	Original	New	Original	New
OriPC_OriDecomOriCH4 (Baseline)	✓		✓		✓	
NewPC_OriDecomOriCH4		✓	✓		✓	
NewPC_OriDecomNewCH4 <sup>&amp;</sup>		✓	✓			✓
NewPC_NewDecomNewCH4* (NewPC_Optimized) <sup>#</sup> (NewPC_Generic) <sup>§</sup>		✓		✓		✓

<sup>&</sup> “NewCH4” uses the newly modified methane module with default parameterization (see Table S3 in the supplementary file).

1090 \* “NewDecom” means replacing the original temperature- and moisture-dependency functions on decomposition rates with (814) new functions of environmental modifiers as listed in Table S2 in the supplementary file. “NewCH4” here means the newly modified methane module with seven parameterizations (Table S3). The seven CH<sub>4</sub> parameterizations were iteratively applied to the model together with 160 common carbon decomposition schemes that provide good performance for CO<sub>2</sub> flux (i.e., NSE\_CO<sub>2</sub> > 0.5) at all the sites. This resulted in 1934 “NewPC\_NewDecomNewCH4” simulations in total (i.e., 814+160×7 = 1934).

1095 # “NewPC\_Optimized” is the optimal simulation among the 1934 “NewPC\_NewDecomNewCH4” cases at each site.

§ “NewPC\_Generic” means the simulation with the identified generic parameterization that can be applied to regional simulation. The generic scheme is the common satisfactory scheme that provides the best overall performance for all the sites.

1100 **Table 3: Mean absolute error (MAE) of simulated ZCP (days) with the original phase-change scheme (Ori\_PC) and newly resized phase-change scheme (NewPC), and the relative improvement (%) of using the new phase-change scheme compared to the baseline results, calculated as  $100\% \times (\text{MAE\_ZCP\_OriPC} - \text{MAE\_ZCP\_NewPC}) / \text{MAE\_ZCP\_OriPC}$ .**

	BES&CMDL			BEO			ATQ			IVO		
	MAE_ZCP_OriPC (days)	MAE_ZCP_NewPC (days)	Improvement (%)	MAE_ZCP_OriPC (days)	MAE_ZCP_NewPC (days)	Improvement (%)	MAE_ZCP_OriPC (days)	MAE_ZCP_NewPC (days)	Improvement (%)	MAE_ZCP_OriPC (days)	MAE_ZCP_NewPC (days)	Improvement (%)
<b>Layer 1</b>	38.80	31.40	19.07	37.60	33.20	11.70	26.33	13.33	49.37	54.00	51.50	4.63
<b>Layer 2</b>	29.20	14.20	51.37	27.40	12.60	54.01	24.33	5.67	76.71	50.50	37.50	25.74
<b>Layer 3</b>	35.20	18.40	47.73	33.60	16.80	50.00	28.00	9.33	66.67	55.75	30.25	45.74
<b>Layer 4</b>	29.60	10.40	64.86	30.60	10.60	65.36	28.67	9.67	66.28	61.50	30.50	50.41
<b>Layer 5</b>	18.00	11.40	36.67	17.60	10.80	38.64	27.67	17.33	37.35	54.50	22.00	59.63
<b>Layer 6</b>	77.40	12.20	84.24	77.40	13.00	83.20	61.67	36.67	40.54	68.00	14.75	78.31
<b>Layer 7</b>	NaN	NaN	NaN	NaN	NaN	NaN	NaN	NaN	NaN	151.33	46.67	69.16

1105

Table 4: Total CH<sub>4</sub> emissions and CO<sub>2</sub> net flux over three seasonal periods, including the early cold season, cold season, and the warm season. The “ELM\_Optimized” here means ELM\_NewPC\_Optimized (Table 2). The percentage of each seasonal total CH<sub>4</sub> emissions to the annual total is included in the brackets.

Total CH <sub>4</sub> Emissions (gC m <sup>-2</sup> )	BES/CMDL			BEO			ATQ		
	Early Cold Season (Sep. and Oct.)	Cold Season (Sep. to May)	Warm Season (Jun. to Aug.)	Early Cold Season (Sep. and Oct.)	Cold Season (Sep. to May)	Warm Season (Jun. to Aug.)	Early Cold Season (Sep. and Oct.)	Cold Season (Sep. to May)	Warm Season (Jun. to Aug.)
<b>ELM_Baseline</b>	0.08 (4.7%)	0.08 (5.1%)	1.53 (94.9%)	0.09 (5.5%)	0.10 (6.2%)	1.54 (93.8%)	0.16 (15.1%)	0.16 (15.3%)	0.89 (84.7%)
<b>ELM_Optimized</b>	0.51 (17.8%)	1.00 (34.8%)	1.88 (65.2%)	0.73 (22.8%)	1.11 (35.0%)	2.07 (65.0%)	0.18 (18.2%)	0.58 (33.4%)	1.16 (66.6%)
<b>Observation</b>	0.63 (21.0%)	1.32 (44.5%)	1.65 (55.5%)	0.83 (24.4%)	1.43 (41.9%)	1.97 (58.1%)	0.36 (19.2%)	0.85 (44.7%)	1.04 (55.3%)
<b>Bias of ELM_Baseline</b>	0.55	1.24	0.13	0.74	1.32	0.43	0.20	0.69	0.16
<b>Bias of ELM_Optimized</b>	0.11	0.32	-0.23	0.10	0.31	-0.09	0.05	0.27	-0.11
<b>Bias Reduction</b>	79.7%	74.2%	-	86.1%	76.5%	-	77.4%	61.3%	-
Total CO <sub>2</sub> Net Flux (gC m <sup>-2</sup> )	BES/CMDL			BEO			ATQ		
	Early Cold Season (Sep. and Oct.)	Cold Season (Sep. to May)	Warm Season (Jun. to Aug.)	Early Cold Season (Sep. and Oct.)	Cold Season (Sep. to May)	Warm Season (Jun. to Aug.)	Early Cold Season (Sep. and Oct.)	Cold Season (Sep. to May)	Warm Season (Jun. to Aug.)
<b>ELM_Baseline</b>	31.27	31.38	2.03	30.99	31.14	13.91	40.46	40.86	-26.05
<b>ELM_Optimized</b>	37.97	75.36	-74.27	47.14	83.71	-47.15	50.51	76.18	-39.64
<b>Observation</b>	43.60	87.50	-67.61	28.20	96.14	-64.33	24.29	58.64	-62.41
<b>Bias of ELM_Baseline</b>	12.33	56.12	-69.64	-2.79	64.99	-78.24	-16.16	17.78	-36.36
<b>Bias of ELM_Optimized</b>	5.63	12.14	6.66	-18.94	12.42	-17.19	-26.21	-17.54	-22.76
<b>Bias Reduction</b>	54.4%	78.4%	109.6%	-	80.9%	78.0%	-	-	37.39%

**Table 5: Historical trend of ZCP durations (days year<sup>-1</sup>) for each soil layer from 1950 to 2017. (Trends with p > 0.05 are not statistically significant.)**

	BES/CMDL		BEO		ATQ	
	Trend (days yr <sup>-1</sup> )	p Value	Trend (days yr <sup>-1</sup> )	p Value	Trend (days yr <sup>-1</sup> )	p Value
ZCP Duration of Layer 1	0.02	0.74	-0.02	0.68	0.07	0.39
ZCP Duration of Layer 2	0.10	0.02	0.10	0.03	0.12	0.09
ZCP Duration of Layer 3	0.13	0.01	0.10	0.04	0.15	0.04
ZCP Duration of Layer 4	0.09	0.14	0.10	0.07	0.21	0.01
ZCP Duration of Layer 5	0.07	0.28	0.10	0.10	0.22	0.03
ZCP Duration of Layer 6	0.98	0.39	0.35	0.56	0.49	0.00

1115

**Table 6: Historical trend (1950 - 2017) in site-scale heterotrophic respiration, CH<sub>4</sub> emission, and CO<sub>2</sub> flux during the ZCP duration at 12 cm (4<sup>th</sup> layer), cold-season months (Sep. - May), and the whole annual cycle (Sep. – Aug.). (Trends with p > 0.05 are not statistically significant.)**

	BES/CMDL		BEO		ATQ	
	Trend of Heterotrophic Respiration					
	Trend (g C m <sup>-2</sup> yr <sup>-1</sup> )	p Value	Trend (g C m <sup>-2</sup> yr <sup>-1</sup> )	p Value	Trend (g C m <sup>-2</sup> yr <sup>-1</sup> )	p Value
<b>ZCP duration at 6 cm</b>	0.14	0.00	0.09	0.04	0.15	0.02
<b>Cold Season (Sep.-May)</b>	0.42	0.00	0.31	0.00	0.41	0.00
<b>Annual (Sep.-Aug.)</b>	0.81	0.00	0.80	0.00	1.06	0.00
	Trend of CH <sub>4</sub> Emission					
	Trend (mg C m <sup>-2</sup> yr <sup>-1</sup> )	p Value	Trend (mg C m <sup>-2</sup> yr <sup>-1</sup> )	p Value	Trend (mg C m <sup>-2</sup> yr <sup>-1</sup> )	p Value
	<b>ZCP duration at 6 cm</b>	-0.20	0.37	-0.71	0.13	-1.69
<b>Cold Season (Sep.-May)</b>	-0.63	0.16	-2.01	0.00	-1.68	0.22
<b>Annual (Sep.-Aug.)</b>	-1.37	0.10	-4.71	0.01	0.52	0.82
	Trend of CO <sub>2</sub> Net Flux					
	Trend (g C m <sup>-2</sup> yr <sup>-1</sup> )	p Value	Trend (g C m <sup>-2</sup> yr <sup>-1</sup> )	p Value	Trend (g C m <sup>-2</sup> yr <sup>-1</sup> )	p Value
	<b>ZCP duration at 6 cm</b>	0.15	0.00	0.12	0.00	0.17
<b>Cold Season (Sep.-May)</b>	0.40	0.00	0.30	0.00	0.36	0.00
<b>Annual (Sep.-Aug.)</b>	0.15	0.43	0.21	0.30	0.29	0.19

1120

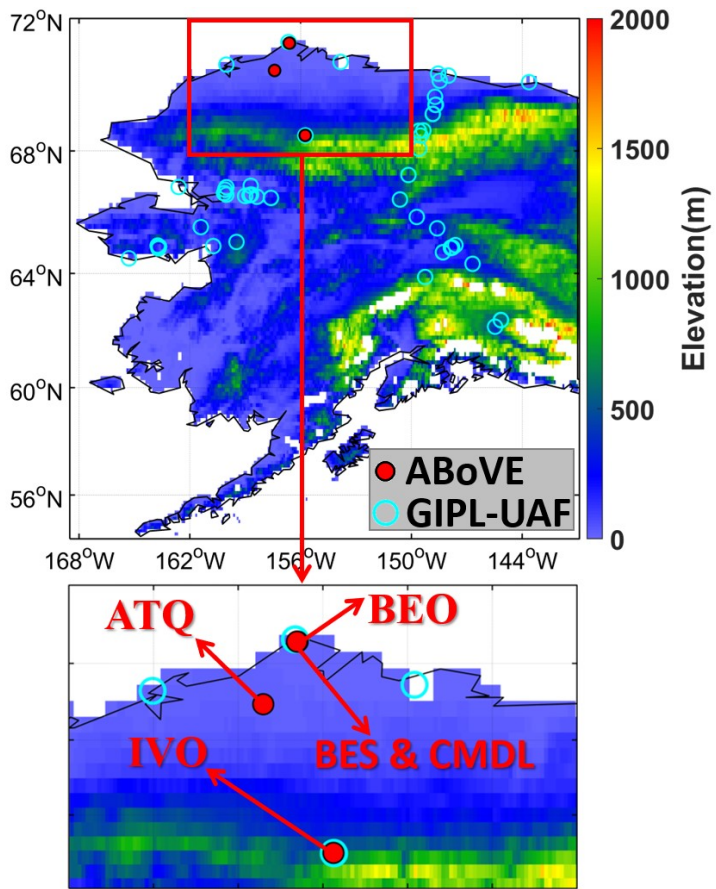
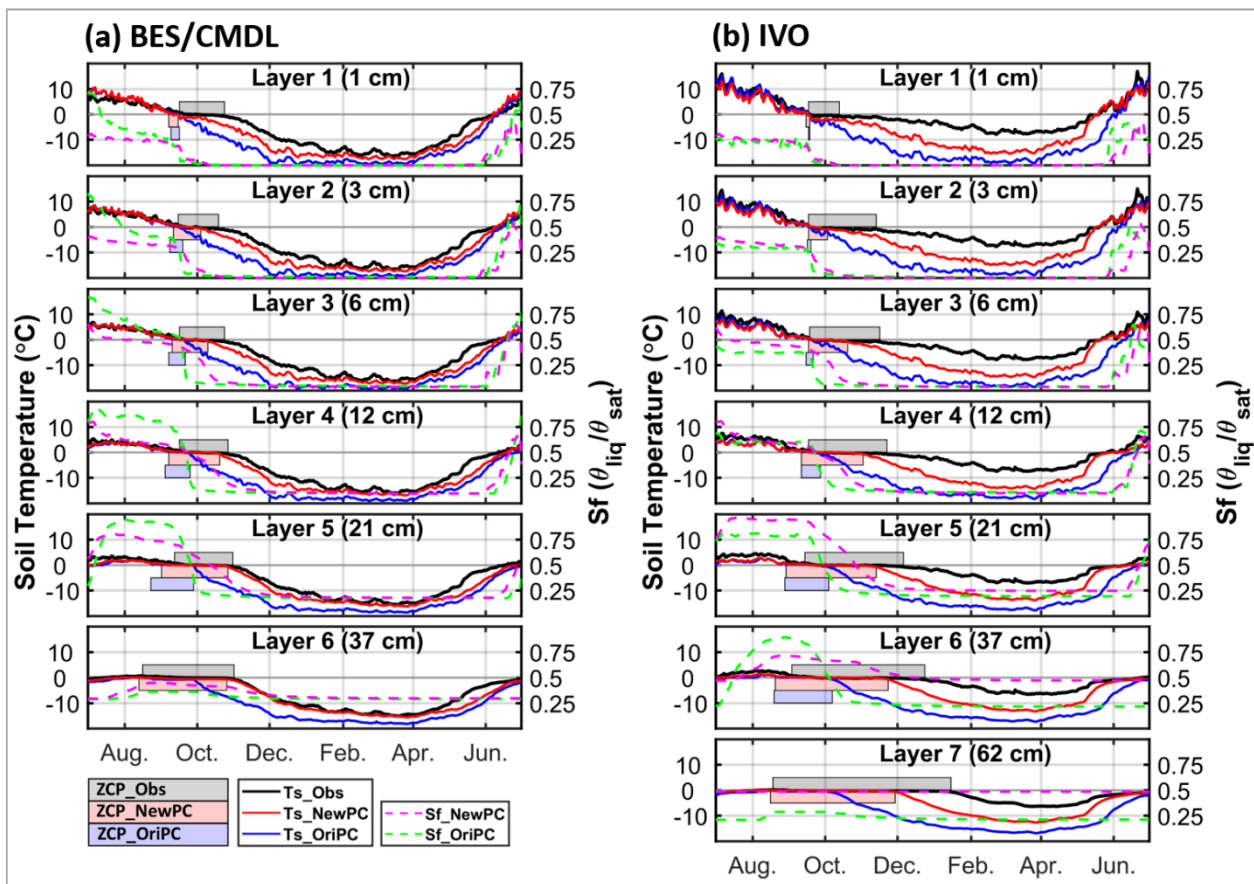


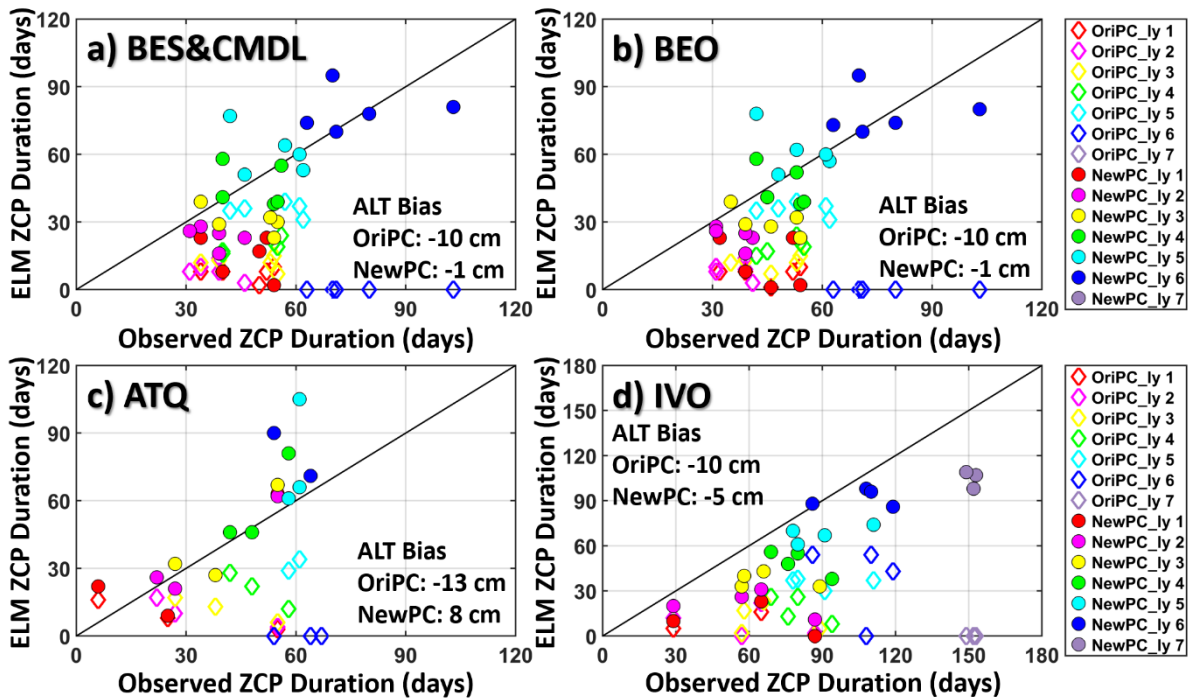
Figure 1: Red dots indicate the five ABoVE flux tower sites used in this study. Cyan circles are GIPL-UAF permafrost sites.



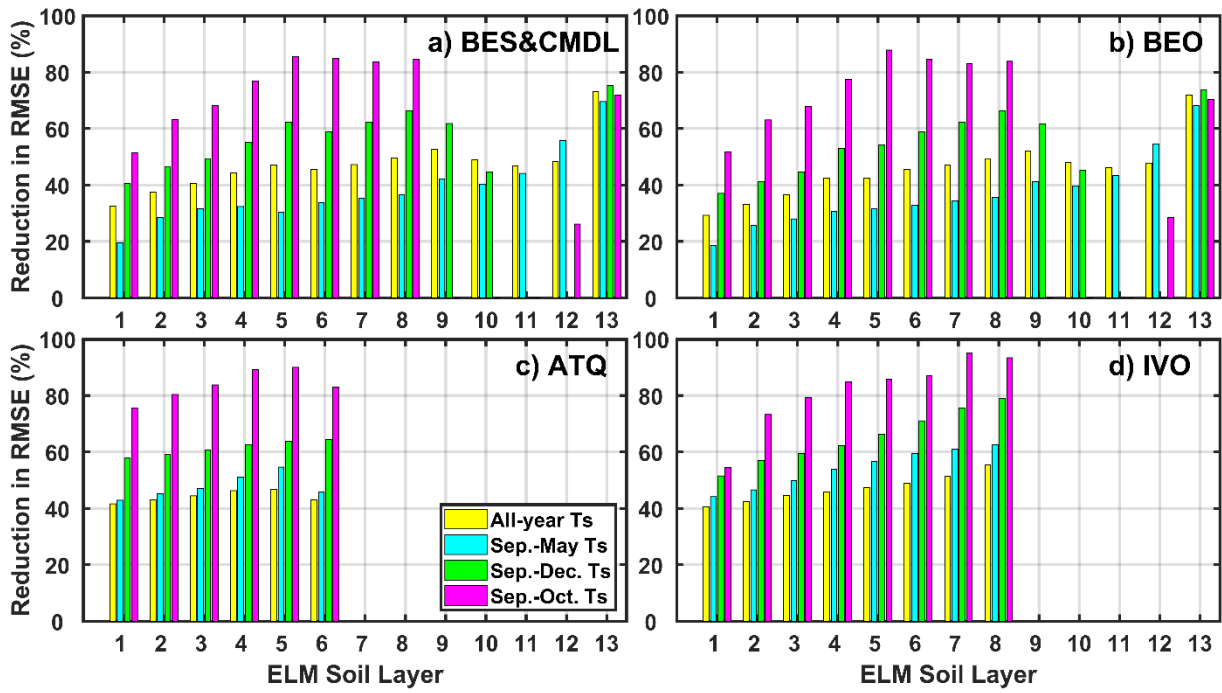
1125

Figure 2: Comparison of multi-year (2013 - 2017) averaged daily soil temperatures observed ( $T_s$ \_Obs, black) and simulated with the original ( $T_s$ \_OriPC, blue) and improved ( $T_s$ \_NewPC, red) phase-change schemes at BES/CMDL (a) and IVO (b). Simulated moisture saturation with the original ( $S_f$ \_OriPC; green) and improved ( $S_f$ \_NewPC; magenta) schemes are shown on the right hand axes. The horizontal axes indicates days from July to June, with ticks represent the first day of each month. Hatched areas represent durations of zero-curtain periods observed (ZCP\_Obs, gray) and simulated (ZCP\_OriPC, blue; ZCP\_NewPC, red). No baseline ZCP is shown in the 6<sup>th</sup> layer for BES/CMDL and the 7<sup>th</sup> layer for IVO because the maximum annual temperature is below 0°C.

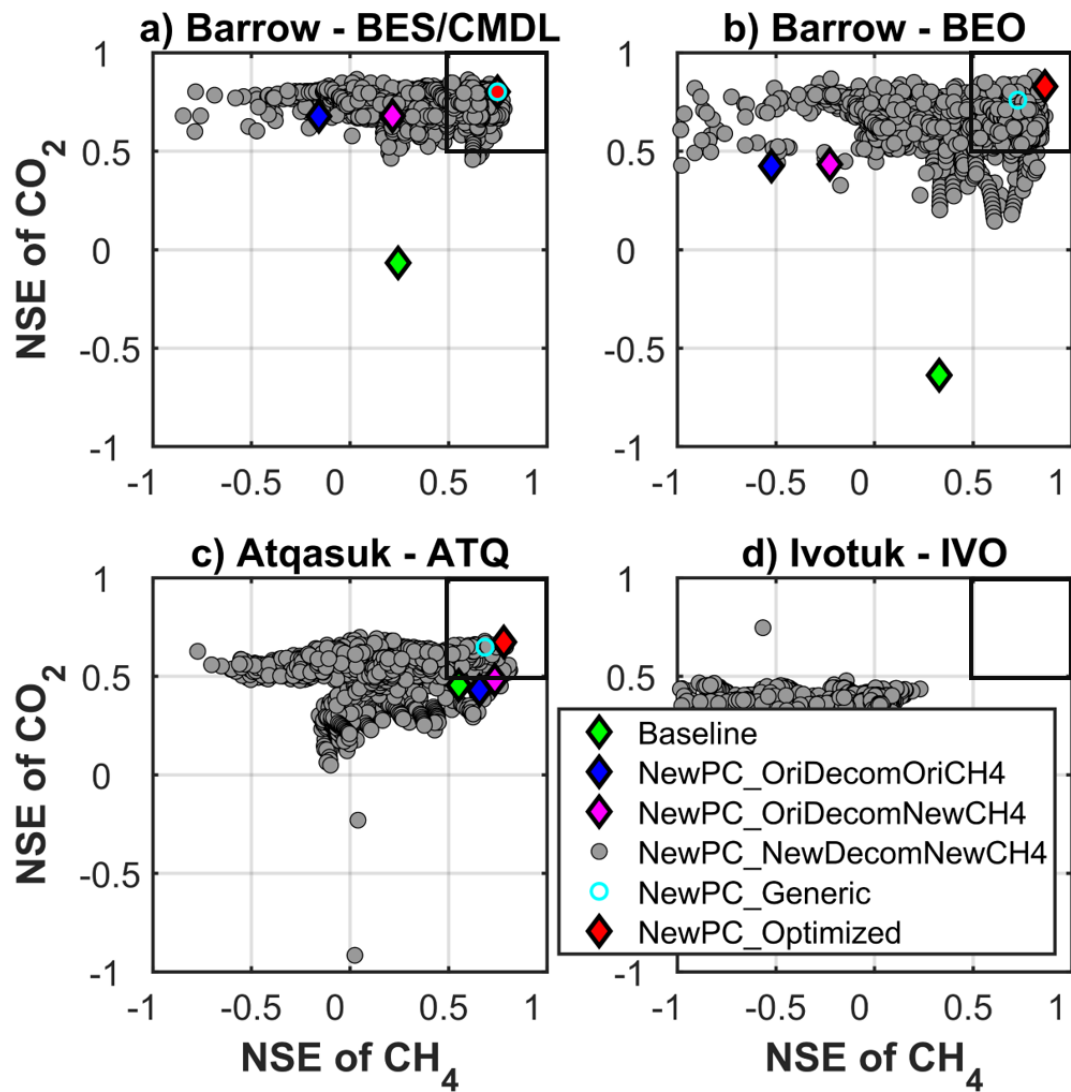
1130



1135 Figure 3: Comparison between observed and ELMv1-ECA simulated durations of ZCP for the original (OriPC; open diamonds)  
 1140 and improved (NewPC; solid circles) phase-change schemes over four annual cycles (July to June) from 2013 to 2017. “ly” means  
 model layer. Simulated ZCP durations with NewPC demonstrate significant improvements compared to OriPC (solid dots vs. open  
 diamonds), especially for the 4<sup>th</sup> to the deepest layer above permafrost. Note, a zero days ZCP means that the maximum daily  
 temperature during an annual cycle is below 0°C. The pairs of zero vs. non-zero days ZCP (e.g., OriPC\_ly 7 at IVO and OriPC\_ly  
 6 at other sites) indicate that baseline results underestimated ALT. The bias (simulation - observation) of multi-year averaged ALT  
 simulated by the two experiments is provided in each panel.



1145 **Figure 4: Relative improvement in the RMSE of simulated soil temperature with the new phase-change scheme (RMSE\_Ts\_NewPC) compared to that with the original scheme (RMSE\_Ts\_OriPC), calculated as  $100\% \times (\text{RMSE\_Ts\_OriPC} - \text{RMSE\_Ts\_NewPC}) / \text{RMSE\_Ts\_OriPC}$ .**



1150 **Figure 5:** Scatter plot between the Nash–Sutcliffe Efficiency (NSE) of simulated monthly CH<sub>4</sub> and CO<sub>2</sub> emissions. An ideal simulation has both NSEs of CH<sub>4</sub> and CO<sub>2</sub> as one (i.e., the upper right corner). The boxes encompass simulations with satisfactory performance (NSE > 0.5). Optimized (red) – the best simulation for each site; Generic (cyan) – the simulation with a common parameterization of carbon decomposition scheme and CH<sub>4</sub> parameter scheme that provides best overall performance for all the sites. See Table 2 for the configuration for each experiment. The grey dots represent all the tested (1934) simulations indicated in the annotation of Table 2. Symbols outside the plotting ranges indicate poor performance, e.g., (-34.9, -0.3) for baseline at IVO, thus are not shown in the figure.

1155

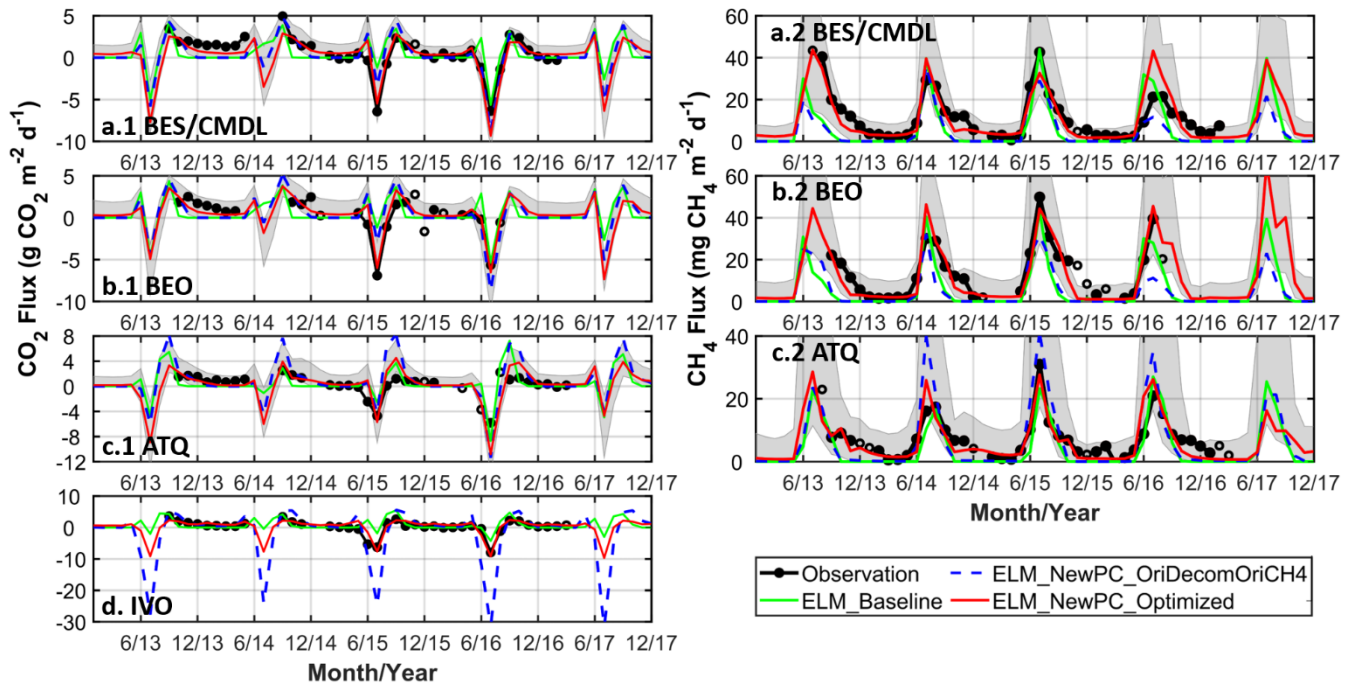
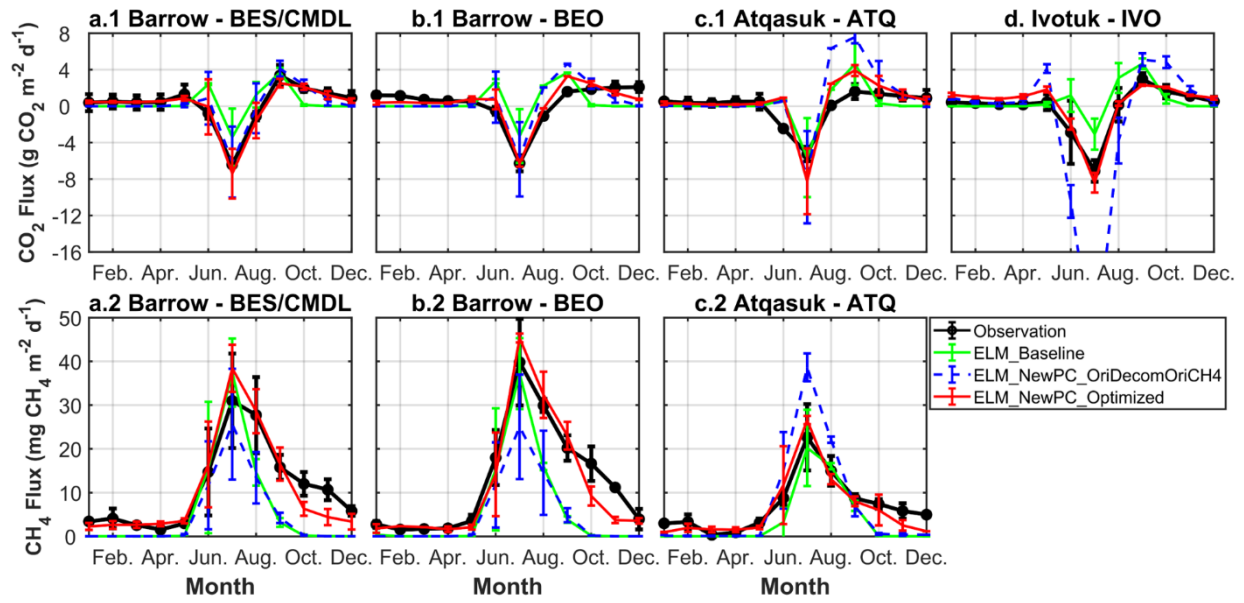


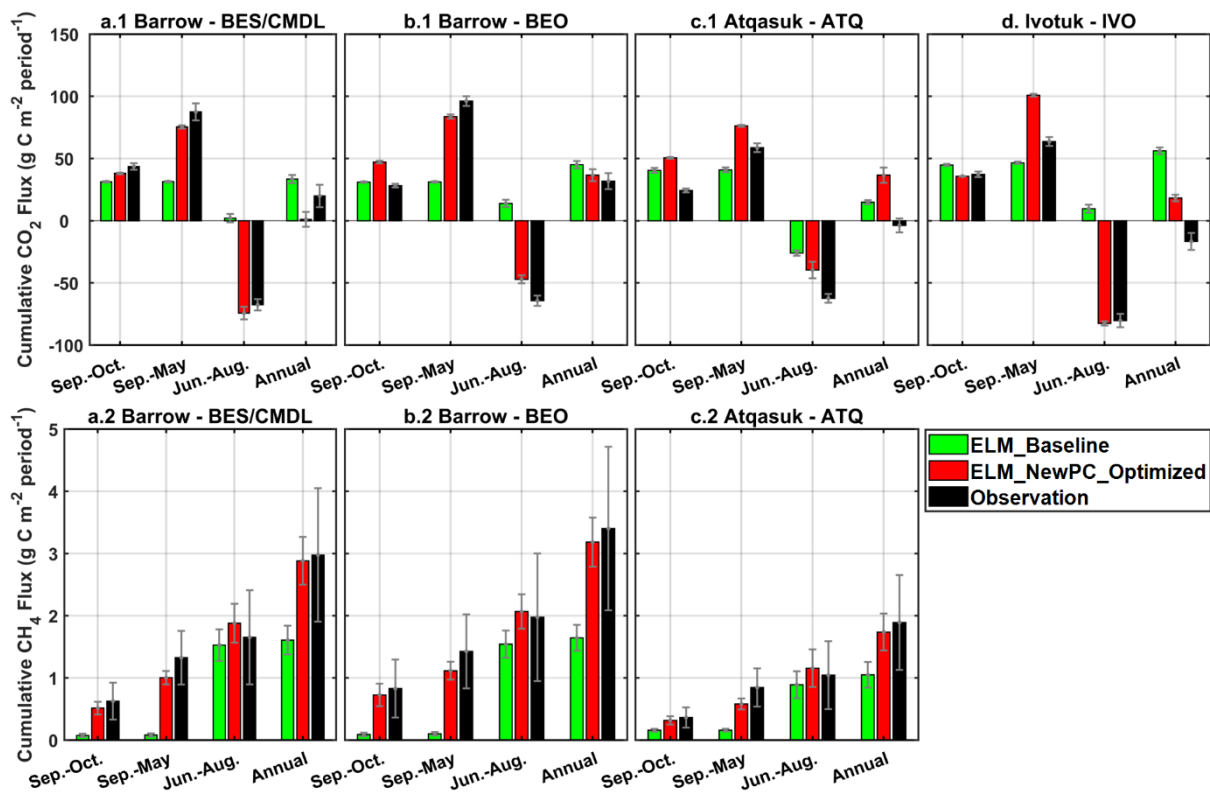
Figure 6: Observed and simulated monthly CO<sub>2</sub> (left) and CH<sub>4</sub> (right) net flux with the baseline model (ELM\_Baseline) and the experiments with updated models (See Table 2 for the configuration for each experiment). Shaded grey areas indicate the minimum-to-maximum bound of simulations within the good performance zone (as shown in Figure 5). Black open circles are observed monthly averages with the number of daily observations less than 10 days, which are not used for the computation in Figure 5. “ELM\_NewPC\_Optimized” means the best simulation for each site (red diamonds in Figure 5). Intermediate results including “ELM\_NewPC\_OriDecomNewCH4” are included in supplementary Figure S8.

1160

1165



**Figure 7: Comparison of multi-year (2013-2017) averaged monthly mean CO<sub>2</sub> net flux (top) and CH<sub>4</sub> emissions (bottom) from simulations and measurements at the study sites. The error bars represent standard deviation of monthly mean.**



1170

Figure 8: Multi-year (2013-2017) averaged total CH<sub>4</sub> emissions (bottom) and CO<sub>2</sub> net flux (top) during the early cold season (Sep. and Oct.), cold-season period (Sep. to May), warm-season period (Jun. to Aug.), and the annual cycle (Sep. to Aug.) at our study sites. Due to the large discontinuity in CO<sub>2</sub> observations, especially over the warm season (shown in Figure 6), the observed annual CO<sub>2</sub> budget is highly uncertain. Still, the cold-season contributions of both CH<sub>4</sub> and CO<sub>2</sub> emissions are greatly improved by the optimized ELMv1-ECA (i.e., ELM\_NewPC\_Optimized).

1175